Research article

Augmented photocatalytic degradation of Acetaminophen using hydrothermally treated g-C$_3$N$_4$ and persulfate under LED irradiation

Smita Gupta [a], Jemi Gandhi [a], Santosh Kokate [a,b], Laxman G. Raikar [a], Vijayakumar Gupta Kopuri [c], Halan Prakash [a,*]

[a] *Energy and Environmental Chemistry Laboratory, Department of Chemistry, Birla Institute of Technology and Science, Pilani, K K Birla Goa Campus, NH17B, Zuarinagar, Goa, 403726, India*
[b] *Aditya Birla Science & Technology Co. Pvt. Ltd., Taloja, Mumbai, 410208, India*
[c] *Kwality Photonics Pvt. Ltd., Kushaiguda, Hyderabad, 500062, India*

ABSTRACT

Photocatalytic degradation of organic pollutants in water using graphitic carbon nitride and persulfate under visible light (g-C$_3$N$_4$/PS system) has been studied. Here, we demonstrate augmentation of photocatalytic degradation of Acetaminophen (AAP) using hydrothermally treated g-C$_3$N$_4$ and PS under 400 nm LED irradiation (HT-g-C$_3$N$_4$/PS system). A pseudo-first-order rate constant (k_{obs}, 0.328 min^{-1}) for degradation of AAP using HT-g-C$_3$N$_4$/PS system was determined to be 15 times higher compared to g-C$_3$N$_4$/PS system (k_{obs}, 0.022 min^{-1}). HT-g-C$_3$N$_4$ showed a higher surface area (81 m^2/g) than g-C$_3$N$_4$ (21 m^2/g). Photocurrent response for HT-g-C$_3$N$_4$ was higher (1.5 times) than g-C$_3$N$_4$. Moreover, Nyquist plot semicircle for HT-g-C$_3$N$_4$ was smaller compared to g-C$_3$N$_4$. These results confirm effective photoelectron-hole separation and charge-transfer in HT-g-C$_3$N$_4$ compared to g-C$_3$N$_4$. AAP degradation using HT-g-C$_3$N$_4$/PS system was significantly inhibited with O$_2^-$ and h$^+$ scavengers compared to ^{1}O$_2$, SO$_4^-$ and HO$^.$ scavengers. ESR results revealed O$_2^-$ formation in HT-g-C$_3$N$_4$/PS system. Moreover, photocurrent measurements reveal AAP oxidation by h$^+$ of HT-g-C$_3$N$_4$ was effective than g-C$_3$N$_4$. HT-g-C$_3$N$_4$ was reused for five cycles in HT-g-C$_3$N$_4$/PS system. Augmented photocatalytic degradation of AAP by HT-g-C$_3$N$_4$/PS system compared to g-C$_3$N$_4$/PS is attributed to effective photoelectron hole separation of HT-g-C$_3$N$_4$ that generates O$_2^-$ and h$^+$ for oxidation of pollutant. Importantly, electrical energy per order (E$_{EO}$) was 7.2 kWh m^{-3} order^{-1}. k_{obs} for degradation of AAP in simulated groundwater and tap water were determined as 0.029 and 0.035 min^{-1}, respectively. Degradation intermediates of AAP were proposed. AAP ecotoxicity against marine bacteria *Aliivibrio fischeri* was completely removed after treatment by HT-g-C$_3$N$_4$/PS system.

1. Introduction

Pharmaceuticals and personal care products (PPCPs) are one of the classes of emerging contaminants found in water resources [1]. Acetaminophen (AAP) is an emerging contaminant belonging to the PPCPs class. AAP is highly consumed pharmaceutical, and it is a

constituent in commonly available over-the-counter non-prescribed as well as prescribed drugs [2–4]. AAP is useful in treating patients with high fever and pain [5]. It is estimated about 1.4×10^5 tons/year of AAP is consumed throughout the world [4]. AAP absorption in the body is estimated to be in the range of 5–15% [6]. Therefore, a large amount of AAP is excreted from the body [2]. AAP has a high solubility of 12.78 g/L in aqueous media [7]. Thus, these facts reveal that AAP has a potential to enter the environment and cause pollution.

Importantly, AAP in treated water, surface water and groundwater have been reported (ng/L - µg/L range) [2,3,8]. Kim et al. reported a hazard quotient of 1.8 for AAP, which indicates AAP may cause an adverse impact on ecological systems [9]. Chlorination of water in presence of AAP is known to yield toxic by-products like 1,4-benzoquinone and N-acetyl-p-benzoquinone imine [10]. All the above facts emphasize the need for effective removal of AAP from water.

Photocatalysis is an important method for degradation of organic pollutants from water. Interestingly, graphitic carbon nitride (g-C_3N_4) is emerging as a visible-light photocatalysts for degradation of organic pollutants in water [11]. g-C_3N_4 is a two-dimensional polymer having a highly delocalized conjugated electronic system consisting of carbon and nitrogen, and acts as a metal-free visible light-absorbing photocatalyst [12]. Notably, g-C_3N_4 is both thermally and chemically stable, with the ability to withstand high temperatures up to 600 °C [11]. Additionally, g-C_3N_4 is reported to be non-toxic toward bacteria [13] and HaCaT cells within g-C_3N_4 doses of 1–10 g/L [14].

Tan et al. [15] reviewed several modification methods of g-C_3N_4, such as nanostructure design, heterostructure construction, metal ion doping, metallic compound coupling, non-metal doping, and carbon material compounding that are useful to enhance the g-C_3N_4 photocatalysis. However, these methods require expensive chemicals, careful synthesis, and g-C_3N_4 modified with metal ions have a potential risk of metal ion leaching and loss of activity [15].

Earlier, alkaline hydrothermal treatment of g-C_3N_4 was reported to be useful for effective photocatalytic oxidation of nitrogen oxides (NOx) compared to g-C_3N_4 [16]. The enhancement in surface area resulting from hydrothermal treatment was proposed to be responsible for the improved photocatalytic activity. Notably, simple hydrothermal treatment of g-C_3N_4 at near neutral pH and its effect on surface area, photo and electrochemical properties, and the photocatalysis performance were not explored. Interestingly, to enhance the photocatalytic activity of g-C_3N_4, persulfate (PS), an effective oxidant was used in g-C_3N_4 photocatalysis (g-C_3N_4/PS system) [17]. In g-C_3N_4/PS system, PS scavenges excited electron in the conduction band to yield reactive radical (O_2^-). As a result, PS retards the electron-hole recombination, thereby also aid in enhancing the available holes for effective photocatalytic degradation by g-C_3N_4/PS system [17].

Additionally, earlier g–C_3N_4 based photocatalysis was mainly studied using a conventional light source (Xenon lamp) with visible light filters for photoexcitation [12,18]. Interestingly, light-emitting diodes (LEDs) are energy-efficient light sources that have gained significant attention in the field of photocatalysis [19,20]. Mainly, LEDs with an emission wavelength around 400 nm is effective for photocatalytic degradation using g-C_3N_4. This is because there is a strong overlap between the 400 nm emission light and the absorption band of g-C_3N_4 that is important for effective photoexcitation [19,21].

The above facts indicate that the HT-g-C_3N_4/PS system that comprises of HT-g-C_3N_4, PS and 400 nm LED irradiation source, may be more effective for photocatalytic removal of emerging contaminants in comparison to g-C_3N_4/PS system. Thus, in this study, we investigated the photocatalytic degradation of AAP using HT-g-C_3N_4/PS system. Characterisation of HT-g-C_3N_4, the rate constant (k_{obs}) for photocatalytic degradation, effect of reactive species scavengers on the k_{obs} values, electron spin resonance, photocurrent, electrochemical measurements results are presented. The degradation pathway of AAP was also analyzed using liquid chromatography-mass spectrometry (LC-MS). Additionally, the electrical energy per order (E_{EO}) values, and the ecotoxicity evaluation of AAP before and after treatment with the HT-g-C_3N_4/PS system using the bioluminescent bacterium *Aliivibrio fischeri* (*A. fischeri*) were conducted.

2. Materials and methods

2.1. Chemicals

Melamine 99% was purchased from Alfa Aesar, UK. Potassium persulfate (99%) was obtained from SD fine chemicals, India. AAP (98%), tert-Butanol (99%), and 1,4-Benzoquinone (98%) were purchased from Loba Chemie Pvt. Ltd, India. Ethylenediamine tetraacetic acid disodium hydrate (99%) was purchased from Himedia, India. Sodium azide 99% was obtained from s d fine chemicals. Buffer solutions (pH 4.00, 7.00, and 10.01) were procured from Thermo Fischer Scientific, India. Methanol, Acetonitrile and Formic acid, were of HPLC grade and purchased from FINAR chemicals, India. Sodium sulfate (99.5%) is used as an electrolyte for photocurrent measurement and was bought from Qualigens, India. Dimethyl-1-pyrroline-N-oxide (DMPO) and 2,2,6,6-tetramethylpiperidine (TEMP) were purchased from Tokyo Chemical Industry Co., Ltd. (TCI), India. All the solutions were prepared using RO water (conductivity 4.0–5.4 µS/cm).

2.2. Preparation of photocatalyst

The g-C_3N_4 photocatalyst was synthesized by thermally decomposing melamine, following reported literature [12]. The preparation of g-C_3N_4 involved taking 15.3 g of melamine powder and placing it in a cylindrical alumina crucible with a lid. The crucible was then placed in a muffle furnace and heated to 575 °C at a heating rate of 5 °C/min. The temperature was maintained at 575 °C for 1.5 h. After calcination the sample was subsequently cooled to room temperature while still inside the furnace. The final product was a

pale-yellow colored material with a yield of 51% (7.827 g of g-C_3N_4 obtained from 15.3 g of melamine), which was then ground into a fine powder and stored as g-C_3N_4 for further use. This material was later characterized and utilized in degradation reactions.

HT-g-C_3N_4 photocatalyst was synthesized by slightly modifying the reported method [16]. The detailed procedure is as follows: The g-C_3N_4 (1 g) was added to 50 ml of RO water, and the suspension was stirred for 30 min followed by 30 min sonication. The sonicated mixture was transferred into a teflon-lined stainless-steel autoclave with a 100 ml capacity and kept in an oven, and heated at 180 °C for 12 h. The resulting product was separated by centrifugation and washed with distilled water and ethanol, respectively. Finally, the product was dried in an oven at 70 °C for 8 h. The whitish-yellow color product was obtained with a yield of 64% and was labeled as HT-g-C_3N_4 (0.640 g of HT-g-C_3N_4 obtained from 1 g of g-C_3N_4). Additionally, HT-g-C_3N_4 was synthesized at 140 °C and 160 °C hydrothermal temperatures following a similar process. However, the degradation activity of AAP by HT-g-C_3N_4 at 180 °C was found to be efficient compared to HT-g-C_3N_4 synthesized at 140 °C and 160 °C.

2.3. Characterization

The surface morphology and elemental composition of the material was analyzed using a Quanta FEG 250 field emission scanning electron microscope (FE-SEM) equipped with area mapping energy dispersive X-ray spectrometer (EDS). The Brunauer-Emmett-Teller (BET) surface area, pore size distribution and pore volume were determined through nitrogen adsorption-desorption method using quanta chrome NOVA 1000e at a temperature of −196 °C. In order to study the structural properties of the material, room temperature powder X-ray diffraction (XRD) was performed utilizing a Mini Flex II powder X-ray diffractometer from Rigaku, Japan. The instrument was equipped with Cu Kα radiation (λ = 1.5405 Å) which was used to scan the material in the range of 2θ = 5-80° with a scanning speed of 3°/min. A PerkinElmer Spectrum FT-IR spectrometer was used to record the FT-IR spectra. X-ray photoelectron spectroscopy (XPS) was conducted using a K-Alpha instrument from Thermo Fisher Scientific (UK). A CHNS Vario MICRO Cube elemental analyzer was used to perform elemental analysis. Zeta potentials were measured using a Malvern Zetasizer-V 7.11 [22]. Scavenging experiment was performed using methanol (MeOH), *tert*-butyl alcohol (TBA), sodium azide (NaN$_3$), ethylenediamine tetra acetic acid (EDTA), and 1,4-benzoquinone (BQ) as radical quenching agents.

For TOC measurements, each time fresh 25 ml of 10 ppm AAP solution was taken and PS and HT-g-C_3N_4 was added and reaction was carried out at different time intervals. The reaction was stopped at different time intervals (0, 1, 2 and 3 h), the entire 25 ml solution was centrifuged to separate the catalyst and was further taken for TOC measurements.

Electron spin resonance (ESR) was recorded using JEOL, ESR Spectrometer. DMPO (60 mM) and TEMP (60 mM) were used for spin-trap. HT-g-C_3N_4 (0.4 g/L) and PS (0.6 mM) were stirred in water and irradiated at 400 nm LED. Samples were withdrawn after 5 or 10 min, filtered through a 0.2 μm filter, and the sample solutions were analyzed for ESR. Microwave frequency, microwave power, and magnetic field were 9.440 GHz, 0.995 mW, and 336 mT, respectively.

The photocurrent response of the synthesized g-C_3N_4 and HT-g-C_3N_4 materials was measured using a three-electrode electrochemical cell system. The working electrodes, g-C_3N_4 and HT-g-C_3N_4, were coated on Indium Tin oxide slides using alcoholic Nafion and a photocatalyst slurry, and were dried in an oven at 120 °C. Ag/AgCl (saturated KCl) electrode and a carbon electrode were used as the reference and counter electrodes, respectively. The photocurrent response was measured using a 10 ml solution of 0.1 M Na$_2$SO$_4$ electrolyte and a 400 nm LED light source. The voltage was set at 0.6 V vs. Ag/AgCl, and the photocurrent response was measured using the IVIUMSTAT electrochemical workstation [23–25].

Fluorescence spectrophotometer (JASCO FP-8500) was employed to acquire photoluminescence (PL) spectra of the photocatalysts by using an excitation wavelength at 335 nm. UV–visible diffuse reflectance spectra (UV-DRS) were measured using a Shimadzu UV-2450 spectrometer, with BaSO$_4$ as a reference. The spectra were measured over a range of 200–800 nm. The Tauc's plot were obtained from UV-DRS spectra [69]. The flat band potential (E_{fb}) of a semiconductor was determined by the Mott-Schottky curve [26,27]. The Mott-Schottky experiment was performed in a potential range of 0–1.0 V (vs. Ag/AgCl) at selected frequencies of 1.0, 1.2 and 1.5 kHz. The E_{fb} values of the g-C_3N_4 and HT-g-C_3N_4 photocatalysts were determined using the Mott-Schottky plot method, with Ag/AgCl as the reference electrode. Specifically, the x-intercept at the tangents of the Mott-Schottky plot was used to calculate the E_{fb} (vs. Ag/AgCl) values. The measured E_{fb} (vs. Ag/AgCl) was converted to a reversible hydrogen electrode (RHE) scale according to Eq. (1) [28]:

$$E_{RHE} = E_{Ag/AgCl} + E^o_{Ag/AgCl} + 0.0592 \text{ pH} \tag{1}$$

Where E_{RHE} is the reverse hydrogen electrode potential (vs. RHE), $E_{Ag/AgCl}$ is the experimentally measured potential against Ag/AgCl reference, and $E^o_{Ag/AgCl}$ = 0.198 V at 25 °C (reference electrode potential in saturated KCl solution) at pH 6.8 (0.1 M Na$_2$SO$_4$). The energy difference (E_d) between E_{fb} (vs. RHE) and valence band (VB) was measured by XPS VB spectrum. The valence band potential (E_{VB}) and conduction band potential (E_{CB}) can be obtained by following Eqs. (2) and (3) [29].

$$E_{VB} = E_d + E_{fb} \tag{2}$$

$$E_{CB} = E_{VB} - E_g \tag{3}$$

The electrochemical impedance spectroscopy (EIS)-Nyquist plot was obtained by applying a sine wave with an amplitude of 10.0 mV across a range of frequencies from 0.01 Hz to 5 MHz.

The solution pH was measured with a EUTECH pH 700 m, India. The pH meter was calibrated using the standard buffer solutions (pH 4.00, 7.00, and 10.01). The initial pH of the AAP solution was adjusted using 0.1 M H$_2$SO$_4$ or 0.1 M NaOH.

2.4. Photocatalytic degradation experiments

25 ml of 10 ppm AAP solution was taken in a 50 ml quartz tube. An LED array that emits 400 nm light was used for the irradiance of solution in a quartz tube (3 LED chips in the array with light focused on the 25 ml solution). The irradiance delivered on the quartz vessel was determined to be 35.85 mW/cm^2. The distance between LED lamp and quartz wall is 0.95 cm (Fig. S1). To the 25 ml of AAP solution, HT-g-C$_3$N$_4$ (0.4 g/L) was added. Then the mixture was stirred, and PS was added to the desired concentration. After addition of PS, immediately the degradation reaction was initiated by switching on the 400 nm LED light. The solution was kept for stirring during the photocatalytic reaction. At appropriate time intervals, 0.5 ml of solution was withdrawn into 2 ml centrifuge tubes containing 5 μL methanol (as a quencher) and centrifuged at 10,000 rpm for 10 min in order to separate the photocatalyst from the solution. The supernatant solution was used for monitoring the AAP concentrations. AAP concentration was analyzed using high-performance liquid chromatography (HPLC Agilent technologies). The calibration curve was made with AAP concentration in the range 1–100 ppb and the Limit of detection and limit of quantification values of HPLC chromatographic method was determined to be 2.62 and 7.95 ng/L respectively (Fig. S7). The column used for HPLC was Phenomenex Kinetex® 2.6 μm EVO C18 100 Å 100 × 4.6 mm. The mobile phase was 15% acetonitrile and 85% water at flow rate of 0.8 ml/min. Intermediates formed during the degradation of AAP were identified by LC-MS (Text S1). In order to check the adsorption-desorption equilibrium is reached reactions were performed in dark conditions, wherein the setup was covered with aluminium foil, and the 400 nm LED light was switched off.

The degradation of AAP in RO water, simulated groundwater, and real tap water was performed, and their E$_{EO}$ values were calculated (Text S2, Table S4). Simulated groundwater was prepared according to an earlier report [30] by addition of the following components to RO water: NaHCO$_3$ (1.2 mM), Na$_2$HPO$_4$ (0.28 mM), Na$_2$SO$_4$ (0.34 mM), NaCl (0.86 mM), Fe (NO$_3$)$_3$·9H$_2$O (0.24 μM), and Resorcinol (9.0 μM). The tap water characteristics are provided in Table S3. For photocatalyst recycling experiments, the photocatalyst was washed and separated by centrifugation and used for next batch without any treatment. All the experiments were performed in triplicates and their standard deviation was determined. All the analyses and graphs were plotted using Origin software version 8.

2.5. Evaluation of the ecotoxicity

The *Aliivibrio fischeri (A. fischeri)* (ATCC 7744), a bioluminescent marine bacteria was used to assess the ecotoxicity of the AAP solution both before and after degradation [31]. The bioluminescence exhibited by the *A. fischeri* bacteria is linked to their cellular respiration activity. Toxic compounds can interfere with bacterial cellular activity, leading to a reduction in bioluminescence. The bioluminescence was measured using a fluorescence spectrophotometer with an excitation lamp switched off (JASCO FP 8500). Before measuring bioluminescence, the pH of all solutions was adjusted to pH ~7 using 0.1 N NaOH. The bioluminescence inhibition was
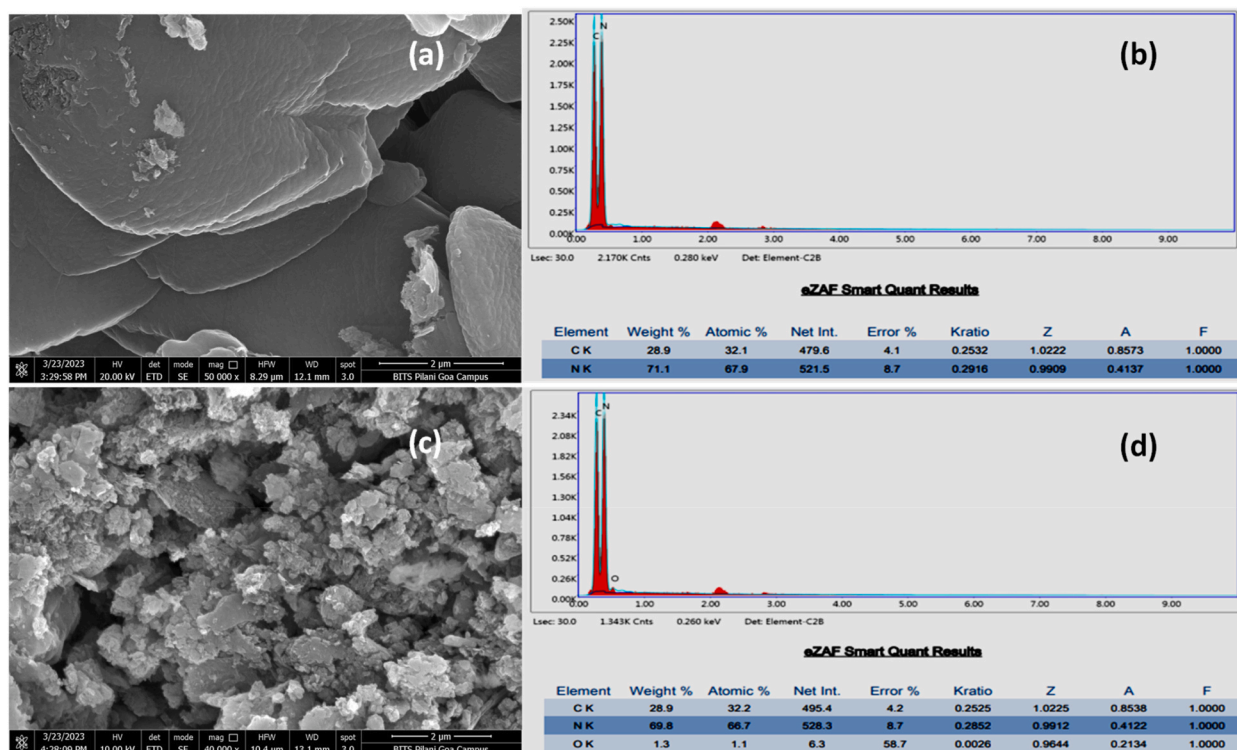

Fig. 1. SEM and EDS of g-C$_3$N$_4$ (a and b); SEM and EDS of HT-g-C$_3$N$_4$ (c and d).

calculated according to Eq. (4), where bioluminescence of control refers to the luminescence of *A. fischeri* in 2% NaCl or persulfate.

$$\text{Bioluminescence inhibition } (\%) = \frac{bioluminescence\ of\ control - bioluminescence\ of\ sample}{bioluminescence\ of\ control} \times 100 \tag{4}$$

3. Results and discussion

3.1. Characterization of HT-g-C$_3$N$_4$

SEM images reveal HT-g-C$_3$N$_4$ have irregular solid agglomerate morphology, whereas g-C$_3$N$_4$ has bulk layered structure (Fig. 1a and c) [32,33]. The EDS spectra of g-C$_3$N$_4$ and HT-g-C$_3$N$_4$ are provided in Fig. 1b and d. The results reveal that both g-C$_3$N$_4$ and HT-g-C$_3$N$_4$ consists of C (atomic weight 32%) and N (atomic weight ~67%) elements with additional O elements (atomic weight 1.1%) in HT-g-C$_3$N$_4$. Additionally, SEM images for hydrothermally treated g-C$_3$N$_4$ at 140 °C and 160 °C temperatures (HT-g–C$_3$N$_4$–140 °C and HT-g–C$_3$N$_4$–160 °C) along with their EDS spectra are provided in Fig. S3.

The specific surface area and pore size distribution of g-C$_3$N$_4$ and HT-g-C$_3$N$_4$ were analyzed using BET surface area with N$_2$ adsorption desorption isotherms (Fig. 2a and b). The specific surface area of HT-g-C$_3$N$_4$ photocatalyst was measured to be 81 m^2/g, while the specific surface area of g-C$_3$N$_4$ was found to be 21 m^2/g. The specific surface area of HT-g-C$_3$N$_4$ was 3.8 times higher than that of g-C$_3$N$_4$ (Table S1) [34]. The N$_2$ adsorption desorption isotherms pore size distribution and pore size distribution for HT-g–C$_3$N$_4$–140 °C and HT-g–C$_3$N$_4$–160 °C was also analyzed (Fig. S4, Table S1). The results reveal that HT-g-C$_3$N$_4$ (180 °C) shows better surface area, higher adsorption-desorption isotherm curve and higher pore volume compared to g-C$_3$N$_4$ and its other modifications which may improve the photocatalytic activity of HT-g-C$_3$N$_4$ photocatalyst.

The XRD pattern of HT-g-C$_3$N$_4$ shows two distinct peaks at 2θ = 13.0° and 27.7°, Fig. 3a [35]. The strong peak at 27.7° was related to interlayer stacking of the (002) melem planes or conjugated aromatic planes. The peak at 13.0° was attributed to the (100) planes corresponding to the in-plane ordering of the repeating nitrogen-linked heptazine units [35]. The XRD pattern of HT-g-C$_3$N$_4$ is similar to g-C$_3$N$_4$ (Fig. 3a) and its other modifications (Fig. S5). These results reveal there is no change in the interlayer distance between carbon nitrides in HT-g-C$_3$N$_4$ compared to g-C$_3$N$_4$. Similar results have been reported for alkaline hydrothermal treatment of g-C$_3$N$_4$ [16].

The FT-IR spectra of HT-g-C$_3$N$_4$ and g-C$_3$N$_4$ shows a sharp peak at 808 cm^{-1}, which is attributed to the heptazine/tri-*s*-triazine ring (Fig. 3b) [36]. Additionally, six sharp peaks in the range of 1200–1700 cm^{-1} corresponding to stretching modes of C–N heterocycles of tri-*s*-triazine skeleton ring were observed [37]. A broad peak ranging from 3000 to 3500 cm^{-1} is attributed to –OH (adsorbed H$_2$O molecules) and N–H vibrations [36]. The FT-IR spectra of HT-g-C$_3$N$_4$ and g-C$_3$N$_4$ photocatalysts did not show any significant differences, according to the obtained results (Fig. 3b).

The blue shift of UV–vis spectra and PL of HT-g-C$_3$N$_4$ (Fig. 3c and d) compared to g-C$_3$N$_4$ is attributed to quantum confinement effect of nano porous structure caused by hydrothermal treatment [38]. Additionally, HT-g-C$_3$N$_4$ showed weaker PL intensity compared to g-C$_3$N$_4$ revealing effective inhibition of photoelectron-hole recombination compared to g-C$_3$N$_4$ [38].

Fig. 4a, shows the XPS survey spectrum and spectra corresponding to core levels, namely C1s, N1s, and O1s of HT-g-C$_3$N$_4$ and g-C$_3$N$_4$ [39]. The two C1s peaks appeared at 281.6 eV (C–N) and 284.8 eV (N═C–N$_2$) (Fig. 4b). The peak at 281.6 eV is indexed to the sp^2 C–N. The peak at 284.8 eV is typically attributed to N═C–N$_2$ of the tri-*s*-triazine unit (Fig. 4b). In N1s, three different peaks were observed at 395.3 eV, 396.9 eV, and 401.5 eV (Fig. 4c). The peaks observed at 396.9 eV and 401.5 eV in the XPS spectra correspond to the sp^2 C═N–C bond of the aromatic triazine ring and the tertiary N atom in the form of N–(C)$_3$, respectively [19]. The peaks in the O1s spectra (Fig. 4d) at about 529.0 eV correspond to C═O [40], and 530.6 eV corresponds to the –OH from hydroxyl on the surface, respectively [41]. Thus, these results reveal no significant difference in the elemental composition of HT-g-C$_3$N$_4$ and g-C$_3$N$_4$. Further,
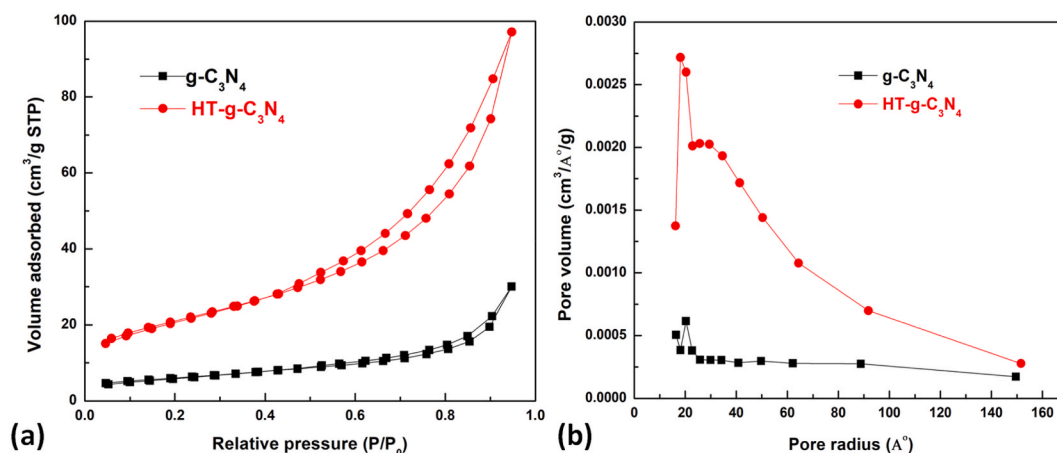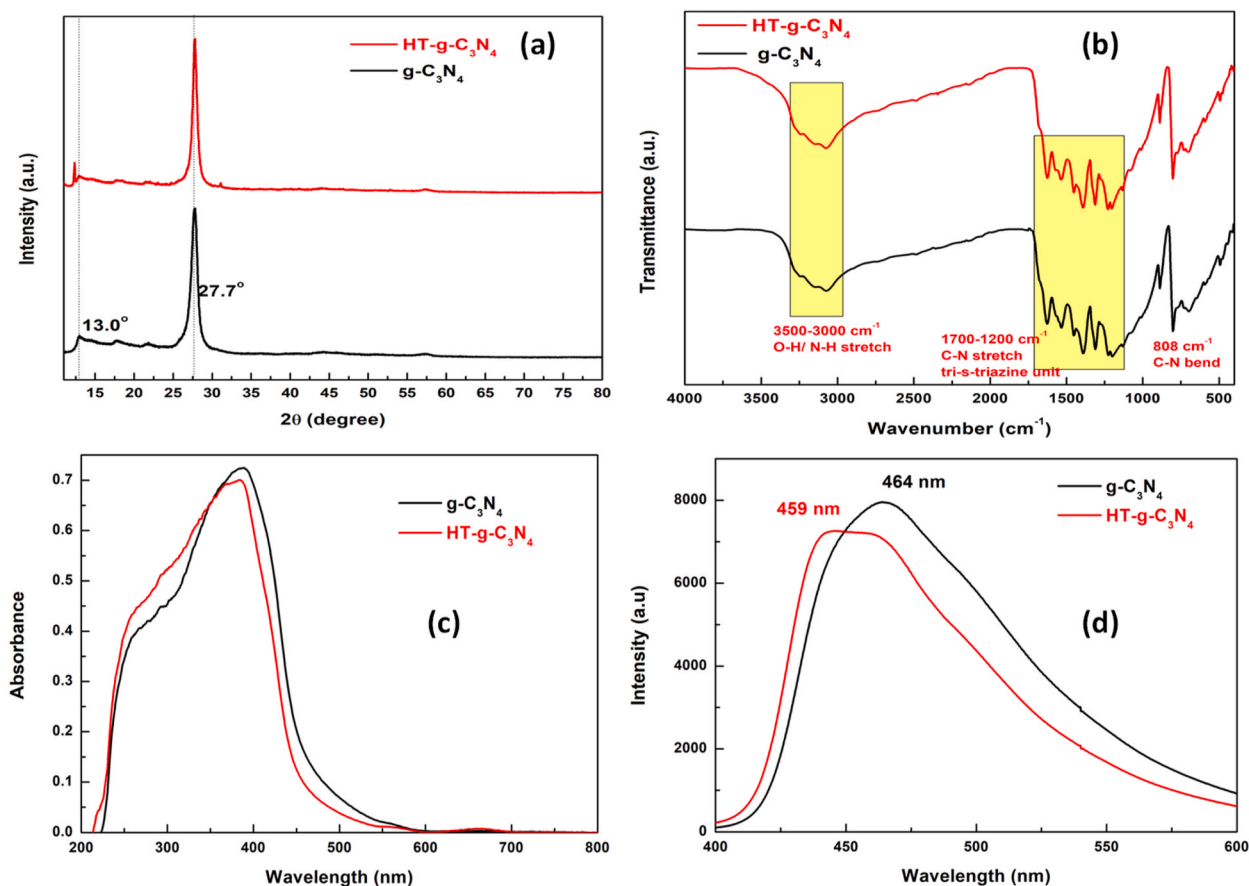

Fig. 2. (a) Nitrogen adsorption and desorption curve (b) BJH pore size distribution plot for g-C$_3$N$_4$, and HT-g-C$_3$N$_4$.

Fig. 3. (a) XRD of g-C_3N_4 and HT-g-C_3N_4 (b) FT-IR of g-C_3N_4 and HT-g-C_3N_4 (c) UV-DRS spectra of g-C_3N_4 and HT-g-C_3N_4 (d) Photoluminescence (PL) emission spectra of g-C_3N_4 and HT-g-C_3N_4.

the CHN analysis results confirm no significant difference in CHN composition with C/N ratio as 0.56 in HT-g-C_3N_4 and g-C_3N_4 (Table S2).
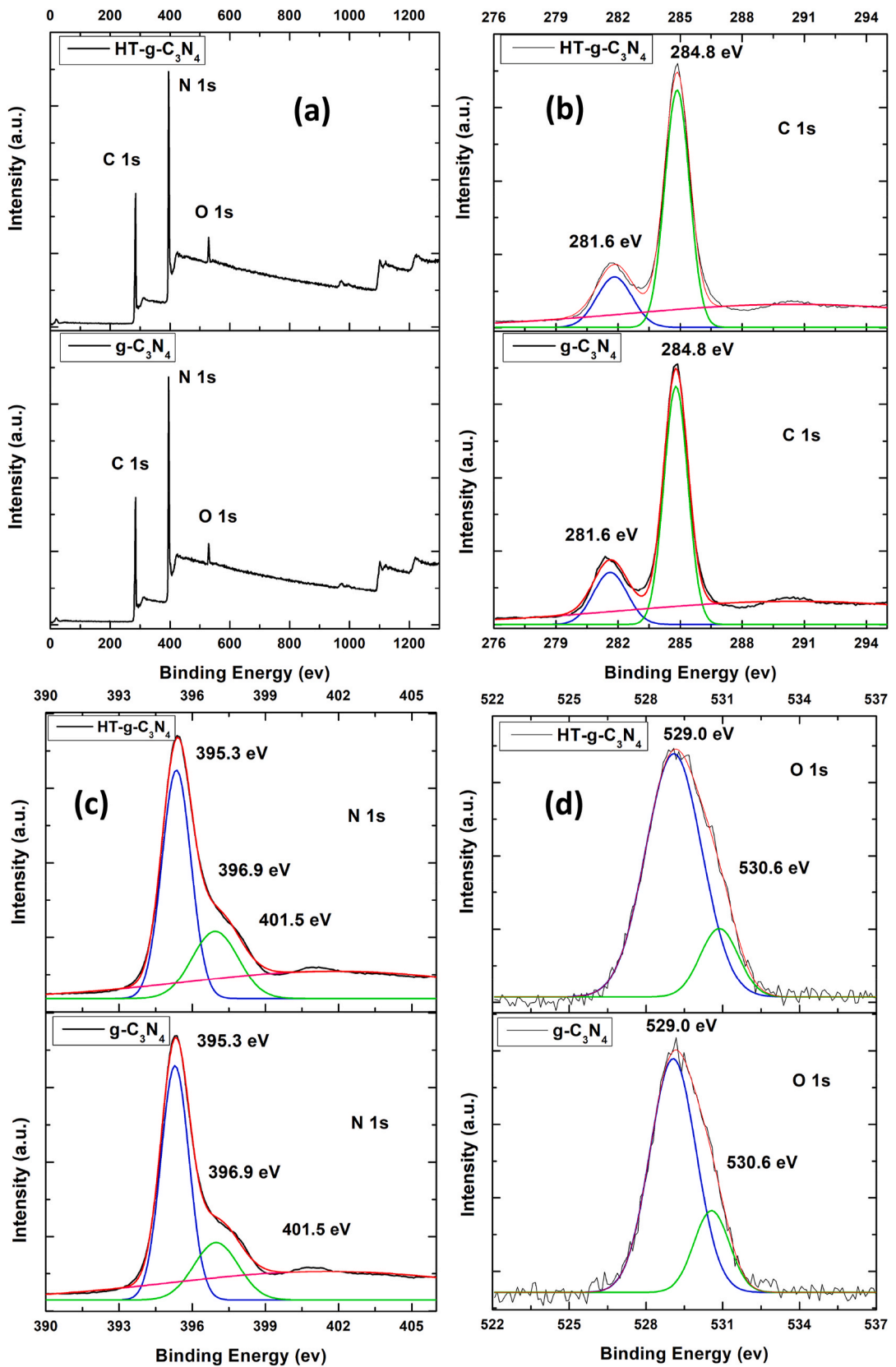
The photocurrent response of HT-g-C_3N_4 photocatalyst was compared to that of g-C_3N_4, as shown in Fig. 5a. Photocurrent response of HT-g-C_3N_4 showed 1.5 times higher photocurrent response compared to g-C_3N_4 (Fig. 5a). This result reveals effective separation of photoelectron and hole in HT-g-C_3N_4. The spectral irradiance profile of 400 nm LED is shown in Fig. S1. HT-g-C_3N_4 shows a strong absorption band around 400 nm (Fig. 3c) and hence effective for photoexcitation and photocatalytic degradation of AAP [19,21].

Tauc's plot reveals the band gap (E_g) values of HT-g-C_3N_4 and g-C_3N_4 to be 2.65 eV and 2.61 eV, respectively (Fig. 6a and b). Both HT-g-C_3N_4 and g-C_3N_4 shows a positive slope in their Mott-Schottky curves revealing these as n type semiconductors (Fig. 6c and d) [42]. The E_{fb} (vs. Ag/AgCl) of HT-g-C_3N_4 and g-C_3N_4 photocatalysts were −1.53 V and −1.28 V (Fig. 6c and d), and their corresponding E_{fb} (vs. RHE) were determined to be −0.929 V and −0.679 V, respectively (Eq. (1)). The E_d values of HT-g-C_3N_4 and g-C_3N_4 were measured to be 2.22 V and 2.11 V respectively (Fig. 6e). The VB potentials of HT-g-C_3N_4 and g-C_3N_4 calculated according to Eq. (2) is 1.291 V and 1.431 V respectively. Hence, the CB potentials of HT-g-C_3N_4 and g-C_3N_4 calculated to be −1.359 and −1.179 V respectively (Eq. (3)) (Fig. 6f) [29]. The EIS-Nyquist plot of HT-g-C_3N_4 showed smaller arc radius compared to g-C_3N_4. This result reveals faster interface charge transfer of HT-g-C_3N_4 than g-C_3N_4 (Fig. 7) [43].

Relatively higher surface area (Table S1), better photocurrent response (Fig. 5) and smaller semicircle (arc radius) in EIS-Nyquist plot (Fig. 7) of HT-g-C_3N_4 compared to g-C_3N_4 indicates that HT-g-C_3N_4 may show a better photocatalytic activity.

3.2. Degradation of AAP by HT-g-C_3N_4/PS and g-C_3N_4/PS systems

Fig. 8a represents the plot of degradation efficiency of AAP vs. time. A complete degradation of AAP occurred within 18 min using HT-g-C_3N_4/PS system, and the k_{obs} for the degradation of AAP was determined to be 0.328 min^{-1} (Table S4). In contrast, the degradation efficiency of AAP was observed to be only 41.0% (k_{obs} = 0.026 min^{-1}) by HT-g-C_3N_4 under 400 nm LED irradiation without PS (Fig. 8a). Importantly, the g-C_3N_4/PS and only g-C_3N_4 without PS under 400 nm LED irradiation showed the AAP degradation efficiency as 40.0% (k_{obs} = 0.022 min^{-1}), and 8.79% (k_{obs} = 0.005 min^{-1}), respectively. Additionally, AAP degradation

(a) HT-g-C₃N₄ and g-C₃N₄: C 1s, N 1s, O 1s
(b) C 1s: 284.8 eV, 281.6 eV
(c) N 1s: 395.3 eV, 396.9 eV, 401.5 eV
(d) O 1s: 529.0 eV, 530.6 eV

(caption on next page)

Fig. 4. XPS spectra of g-C$_3$N$_4$ and HT-g-C$_3$N$_4$ (a) XPS survey (b) C 1s (c) N 1s (d) O 1s.

was negligible under 400 nm LED irradiation in the absence (0.55%, 0.0002 min^{-1}) and presence of PS (4.08%, 0.0024 min^{-1}), as shown in Fig. 8a (light controls).

AAP removal efficiency by (i) dark without PS (0.89%, 0.0003 min^{-1}), ii) dark with PS (2.73%, 0.0011 min^{-1}), iii) dark with g-C$_3$N$_4$ (1.10%, 0.0004 min^{-1}), iv) dark with HT-g-C$_3$N$_4$ (2.20%, 0.0013 min^{-1}), v) dark with g-C$_3$N$_4$ and PS (2.57%, 0.0015 min^{-1}), vi) dark with HT-g-C$_3$N$_4$ and PS (5.21%,0.0029 min^{-1}) were determined to be incomplete Fig. 8b (dark controls). At the optimized condition, E$_{EO}$ for the photocatalytic degradation of AAP by HT-g-C$_3$N$_4$/PS system was found to be significantly lower (7.2 kW h m^{-3} order^{-1}) than g-C$_3$N$_4$/PS system (105.6 kW h m^{-3} order^{-1}) respectively (Text S2, Table S4). Additionally, the performance of HT-g-C$_3$N$_4$ synthesized at hydrothermal temperatures of 140 °C and 160 °C to degrade AAP was investigated (Fig. S2). However, HT-g-C$_3$N$_4$ synthesized at a hydrothermal temperature of 180 °C showed effective degradation of AAP, Fig. 8a and Fig. S2.

Thus, all the above results reveal that the combination of HT-g-C$_3$N$_4$/PS system is an effective system for the degradation of AAP (Fig. 8a) compared to all the control experiments.

3.3. Effect of initial concentration of PS, AAP, and HT-g-C$_3$N$_4$

Fig. 9a shows the effect of initial PS concentrations (0.3–1.2 mM) on degradation of AAP using HT-g-C$_3$N$_4$/PS system. The increase in the initial PS concentration leads to a corresponding increase in the k$_{obs}$ values, Fig. 9b, Table S4. The presence of sulfate radical anion (SO$_4^-$) can be inhibited by PS at higher PS concentrations, as shown in Eq. (5) [44]. Importantly, k$_{obs}$ values increased upon increasing the PS concentration in the range of 0.3–1.2 mM, indicating that Eq. (5) is insignificant within the studied range, Fig. 9b. A similar result was reported for other photocatalytic activation of PS [45].

$$S_2O_8^{2-} + SO_4^- \rightarrow S_2O_8^- + SO_4^{2-} \quad k = 6.1 \times 10^5 \text{ M}^{-1} \text{ s}^{-1} \tag{5}$$

Fig. 10a shows that the degradation efficiency of AAP decreases with an increase in the initial concentration of AAP (5–25 ppm)

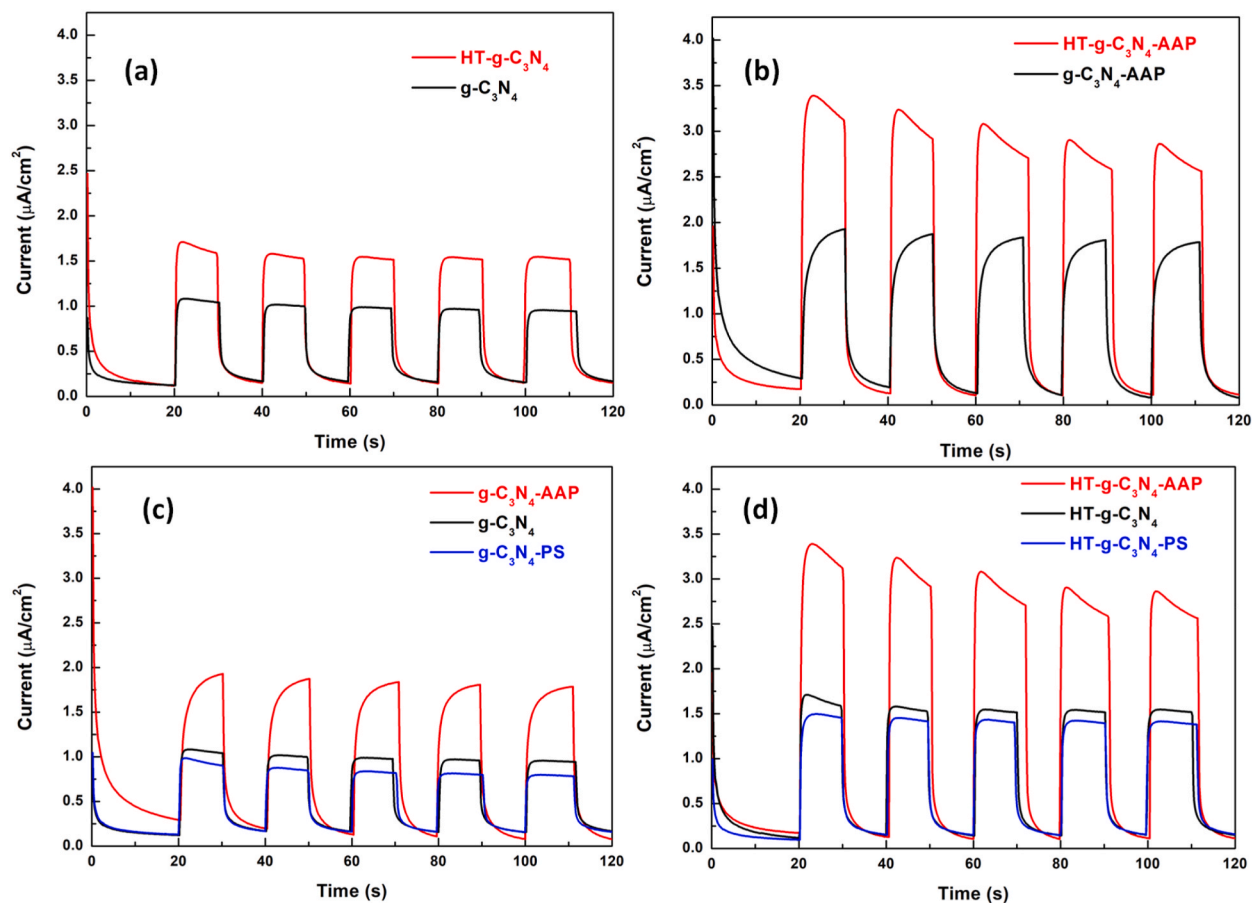**Fig. 5.** Photocurrent-time dependence curve of (a) g-C$_3$N$_4$ and HT-g-C$_3$N$_4$ (b) g-C$_3$N$_4$ and HT-g-C$_3$N$_4$ in presence of AAP (c) g-C$_3$N$_4$ in presence of AAP and PS (d) HT-g-C$_3$N$_4$ in presence of AAP and PS in 0.1 M Na$_2$SO$_4$ solution with a light on/off interval of 20 s at 0.6 V potential.
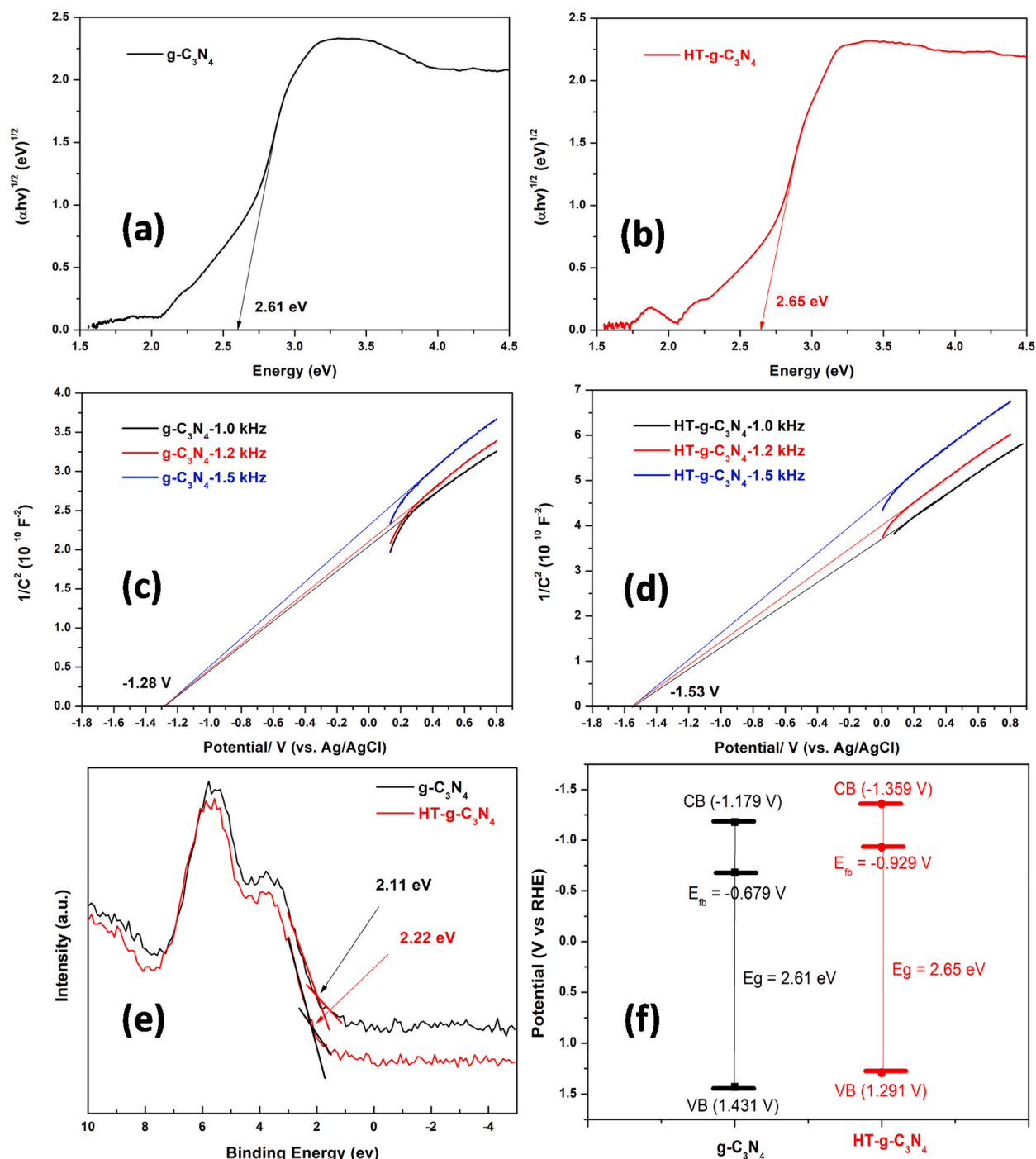
Fig. 6. Tauc's plot of (a) g-C$_3$N$_4$ (b) HT-g-C$_3$N$_4$; Mott-Schottky of (c) g-C$_3$N$_4$ (d) HT-g-C$_3$N$_4$; (e) XPS valence band spectra (f) Band alignments.

using HT-g-C$_3$N$_4$/PS system [46]. The plot k$_{obs}$ vs. AAP concentration (Fig. 10b) clearly shows that the k$_{obs}$ values decreases with an increase in AAP concentration and obeyed a power function (k$_{obs}$ = 3.911[AAP]$_0^{-1.06}$, R^2 = 0.997) [47]. Importantly, as PS to HT-g-C$_3$N$_4$ ratio remains constant, the amount of reactive species generated in the solution stays the same, even if the initial concentration of AAP is increased. Therefore, at higher concentrations of AAP, there is a lower amount of reactive species available for the degradation of AAP, leading to a reduction in the k$_{obs}$ values, Fig. 10b [17,47].

A plot of degradation efficiency vs. time at various initial concentration of HT-g-C$_3$N$_4$ photocatalyst (0.2–0.8 g/L) is shown in Fig. 11a. A plot of k$_{obs}$ vs. HT-g-C$_3$N$_4$ concentration is represented in Fig. 11b. The k$_{obs}$ values exhibit a linear increase with increasing
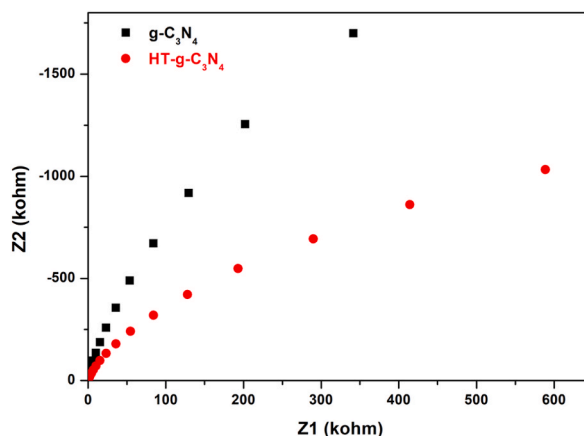
Fig. 7. EIS-Nyquist plot of HT-g-C_3N_4 and g-C_3N_4 obtained by applying a sine wave amplitude of 10.0 mV over the frequency range from 0.01 Hz to 5 MHz.
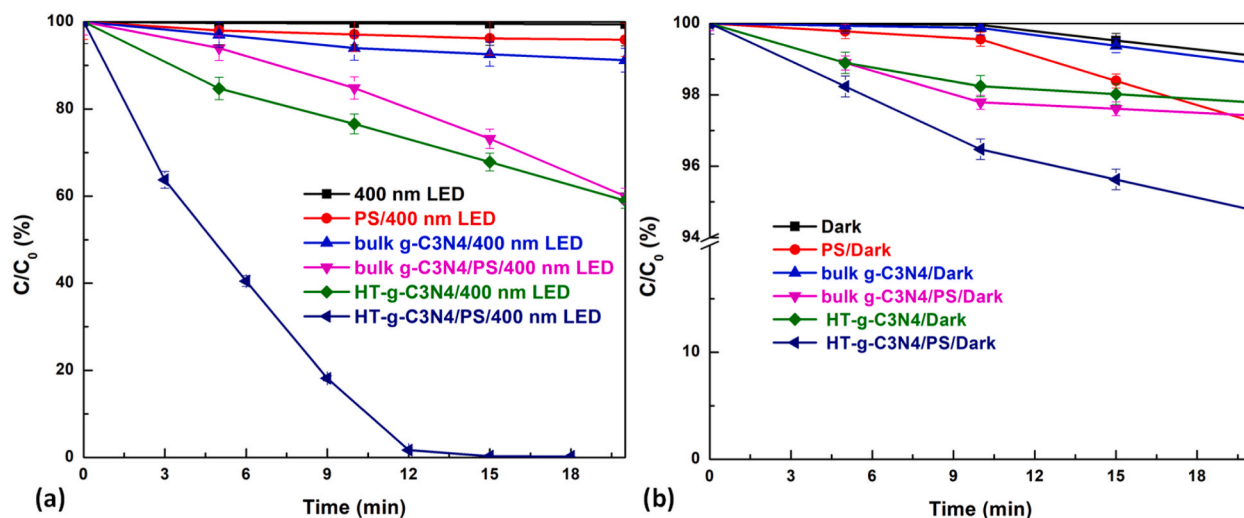

Fig. 8. Degradation efficiency of AAP vs. time plot under different conditions (a) under 400 nm LED condition (b) under dark conditions. [AAP] = 10 ppm, [g-C_3N_4] = [HT-g-C_3N_4]* = 0.4 g/L, [PS] = 0.6 mM, Irradiance = 35.85 mW/cm^2 *synthesized at 180 °C.

concentrations of HT-g-C_3N_4 up to 0.4 g/L, but beyond this concentration, the k_{obs} values remain relatively stable (Fig. 11b, Table S4). The increase in HT-g-C_3N_4 concentration increases the available active sites and enhances the degradation efficiency of AAP. However, at a relatively higher concentration, the solution becomes more turbid, which may affect the availability of light for effective photolysis, leading to a saturation of the k_{obs} values [17]. Under the present experimental conditions, the optimized HT-g-C_3N_4 concentration was determined to be 0.4 g/L (Fig. 11b).

3.4. Effect of initial pH

The photocatalytic degradation of AAP at different initial pH (3-10) values is shown in Fig. 12a. The isoelectronic point of HT-g-C_3N_4 was determined to be 4.6 (Fig. S6). Hence, above pH 4.6, the surface charge of HT-g-C_3N_4 is negatively charged. At pH above 9.38, the AAP exists in negatively charged phenoxide form due to deprotonation of the OH group of phenol (pKa 9.38) [48]. Therefore, under alkaline conditions, at pH 9.38, the k_{obs} values are expected to slightly retard compared to acidic conditions (Fig. 12b) due to the electrostatic repulsion between AAP and HT-g-C_3N_4 [49]. Notably, the HT-g-C_3N_4/PS system for degradation of AAP is applicable in the wide pH range Fig. 12a.
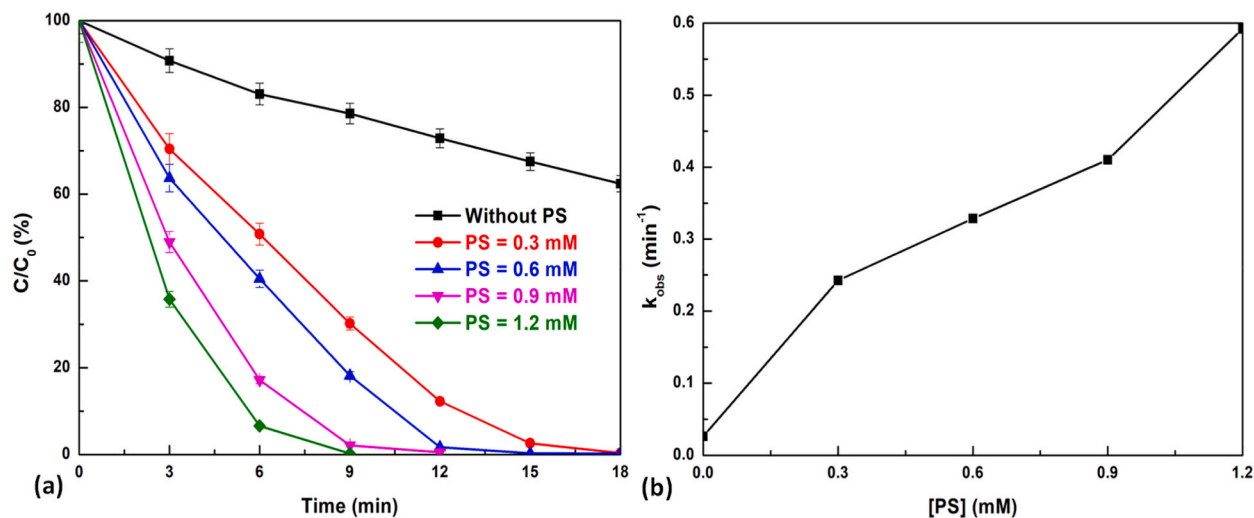
Fig. 9. (a) Effect of initial concentration of PS (b) A plot of k_{obs} vs. initial PS concentration. [AAP] = 10 ppm, [PS] = 0–1.2 mM, [HT-g-C$_3$N$_4$] = 0.4 g/L, Irradiance = 35.85 mW/cm^2.
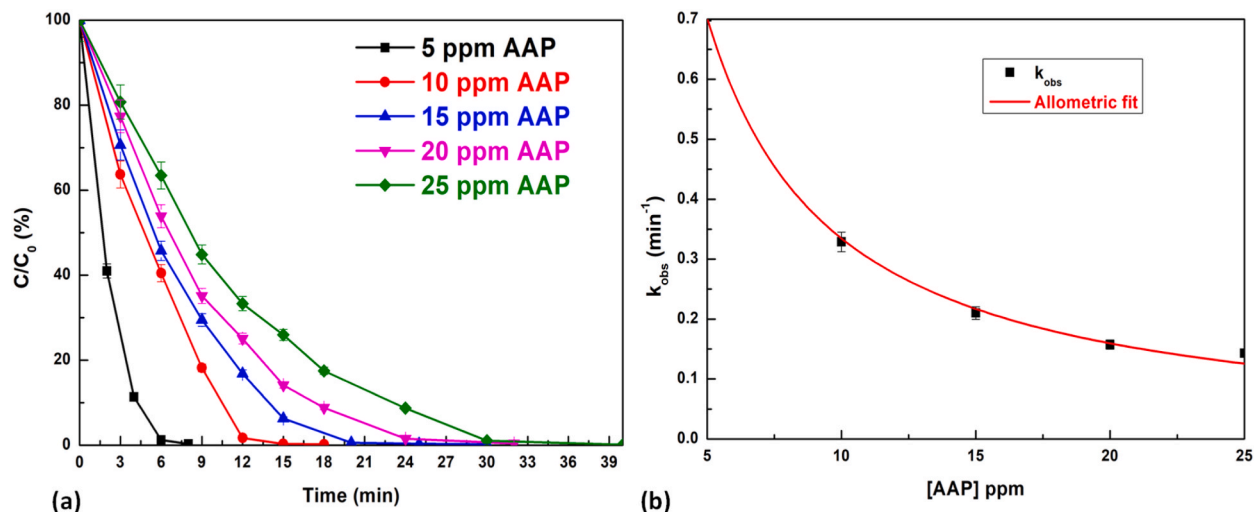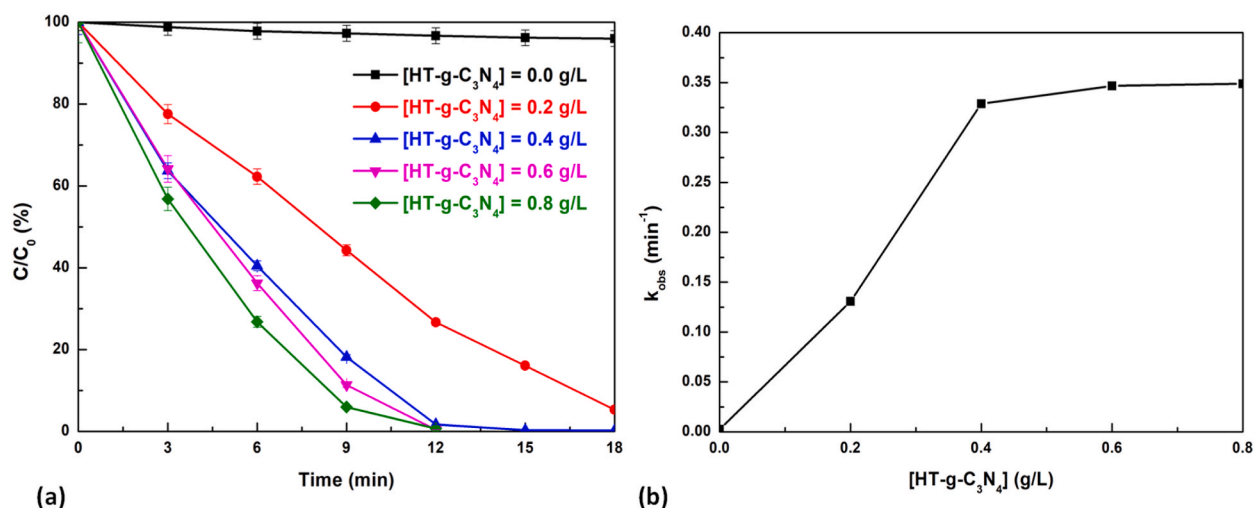

Fig. 10. (a) Effect of initial concentration of AAP (b) A plot of k_{obs} vs. initial concentration of AAP. [AAP] = 5–25 ppm, [HT-g-C$_3$N$_4$] = 0.4 g/L, [PS] = 0.6 mM, Irradiance = 35.85 mW/cm^2.

3.5. Identification of reactive oxidizing species

Under 400 nm LED irradiation, HT-g-C$_3$N$_4$ generates photoexcited electrons (e$^-$) and holes (h$^+$) in its CB and VB, respectively (Eq. (6)). Notably, the presence of BQ, a known quencher of the superoxide radical anion (O$_2^-$), resulted in a significant inhibition of AAP degradation, as shown in Fig. 13. This suggests that the O$_2^-$ is likely involved in the degradation of AAP. The CB potential of HT-g-C$_3$N$_4$ was determined to be more negative (−1.359 V vs. RHE) than the redox potential of E^o (O$_2$/ O$_2^-$) (−0.33 V vs NHE) [50,51] (Fig. 6f). Thus, the photoelectron generated on the CB of HT-g-C$_3$N$_4$ can easily convert adsorbed oxygen to O$_2^-$ according to Eq. (7). Additionally, the ESR spectrum of DMPO-O$_2^-$ adduct further confirms the presence of O$_2^-$ in the HT-g-C$_3$N$_4$/PS system (Fig. 14a).

The inhibition of the degradation of AAP by the HT-g-C$_3$N$_4$/PS system was observed to be insignificant in the presence of SO$_4^-$ scavenger viz., methanol (Fig. 13). Moreover, in ESR, only very weak signals corresponding to SO$_4^-$ was observed under light and dark conditions (Fig. 14b). Thus, these results reveal O$_2^-$ is dominant (Eq. (9)) in the HT-g-C$_3$N$_4$/PS system compared to the SO$_4^-$ (Eq. (10)). A similar result was earlier reported for the photocatalytic activity of g-C$_3$N$_4$ in the presence of PS [17]. S$_2$O$_8^{2-}$ can scavenge the photoexcited e$^-$ in the CB and decompose to produce SO$_4^-$ (Eq. (10)) [52]. However, as discussed above, SO$_4^-$ formation is insignificant, and PS activation to SO$_4^-$ (Eq. (10)) is not the major reaction in HT-g-C$_3$N$_4$/PS system. It is known that PS acts as an e$^-$ mediator and promotes the generation of O$_2^-$ without significant formation of SO$_4^-$ (Eqs. (8) and (9)) [17,52].

Fig. 11. (a) Effect of initial concentration of HT-g-C$_3$N$_4$ photocatalyst (b) A plot of k$_{obs}$ vs. initial HT-g-C$_3$N$_4$ photocatalyst concentration. [AAP] = 10 ppm, [HT-g-C$_3$N$_4$] = 0.4 g/L, [PS] = 0.6 mM, Irradiance = 35.85 mW/cm^2.
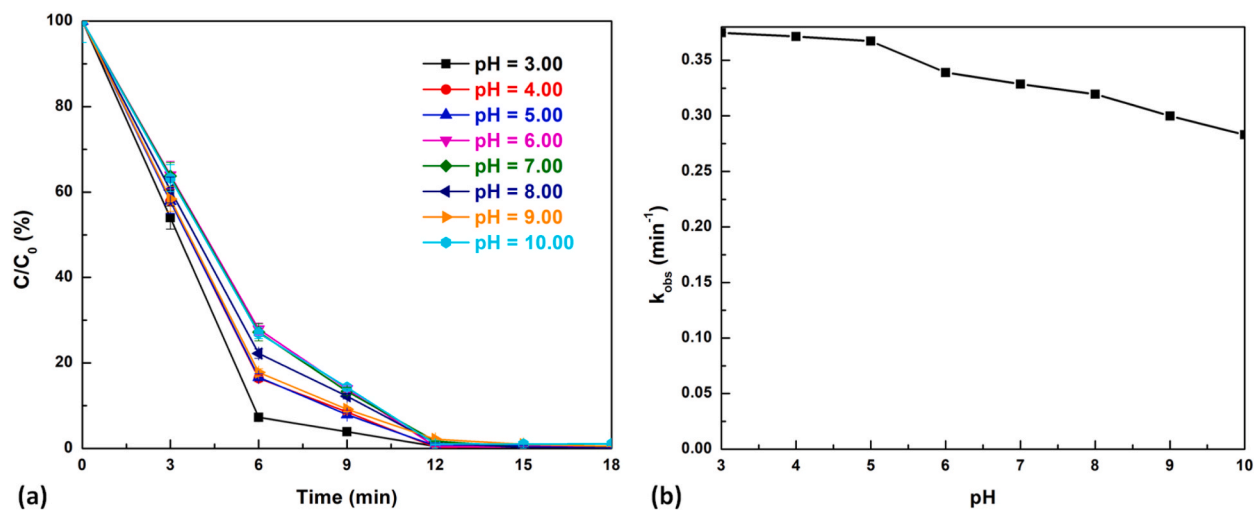

Fig. 12. (a) Effect of initial pH on degradation of AAP (b) A plot of k$_{obs}$ vs. initial pH. [AAP] = 10 ppm, [PS] = 0.6 mM, [HT-g-C$_3$N$_4$] = 0.4 g/L, pH = 3–10, Irradiance = 35.85 mW/cm^2.

Hydroxyl radical (HO$^.$) is hardly generated via the direct oxidation of HO$^-$ ion or H$_2$O molecules by h$^+$ generated at VB of HT-g-C$_3$N$_4$, as the VB edge potential of HT-g-C$_3$N$_4$ (+1.291 V vs. RHE) was determined to be less positive than the redox potential of HO$^.$/HO$^-$ or HO$^.$/H$_2$O (+2.40 and +2.72 V vs. NHE) [50] (Fig. 6f). Importantly, the degradation of AAP was not effectively quenched in the presence of TBA, a HO$^.$ quencher that further emphasizes the formation of HO$^.$ due to the oxidation of HO$^-$/H$_2$O by h$^+$, as well as by the secondary reaction of SO$_4^{.-}$ (Eqs. (11) and (12)) are not the major reactions in HT-g-C$_3$N$_4$/PS system. ESR spectral results also reveal very weak signals that may be due to HO$^.$ or due to the rapid conversion of DMPO-SO$_4^{.-}$ adduct to DMPO-HO$^.$ adduct [53] (Fig. 14b).

ESR spectra shows the presence of TEMP-^{1}O$_2$ adduct (Fig. 14c) that reveals HT-g-C$_3$N$_4$/PS under dark condition generates singlet oxygen (^{1}O$_2$). It is known that carbonaceous materials have the potential to activate PS to produce ^{1}O$_2$. The carbonyl functional groups present on the surface of the photocatalyst were proposed to convert the PS into ^{1}O$_2$ (via a non-radical pathway) [54]. The ESR signal corresponding to TEMP-^{1}O$_2$ adduct in the HT-g-C$_3$N$_4$/PS under 400 nm LED irradiation was almost similar to HT-g-C$_3$N$_4$/PS under dark condition (Fig. 14c). Notably, the degradation of AAP was not effectively quenched in presence of NaN$_3$, a ^{1}O$_2$ scavenger, in comparison to the quenching due to the O$_2^{.-}$ scavenger (Fig. 13). These results reveal that ^{1}O$_2$ generation via a non-radical pathway is not significant and degradation mainly occurs via electron transfer mediated mechanism.

Moreover, the photocatalytic degradation of AAP was effectively quenched in presence of excess EDTA, a h$^+$ scavenger (Fig. 13). This result clearly reveals the h$^+$ are also involved in the oxidation of AAP. Interestingly, the photocurrent was enormously increased in
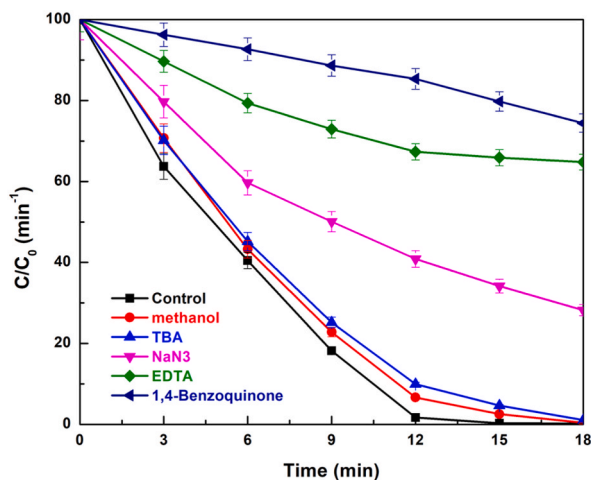
Fig. 13. Reactive species quenching experiments on degradation of AAP [MeOH] = [TBA] = [EDTA] = [BQ] = [NaN$_3$] = 100 mM, [AAP] = 10 ppm, [PS] = 0.6 mM, [HT-g-C$_3$N$_4$] = 0.4 g/L, Irradiance = 35.85 mW/cm^2.
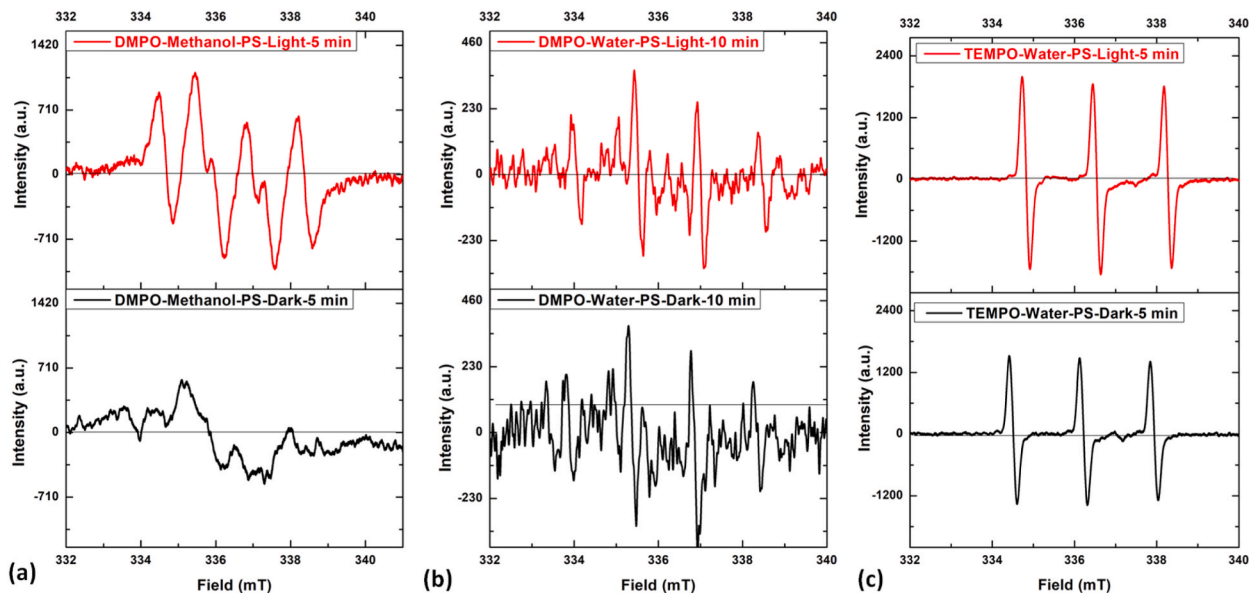
Fig. 14. ESR spectra of (a) DMPO-O$_2^-$ adduct (b) DMPO-HO$^{\cdot}$ and DMPO-SO$_4^-$ adduct (c) TEMP-^{1}O$_2$ adduct. [AAP] = 10 ppm, [PS] = 0.6 mM, [HT-g-C$_3$N$_4$] = 0.4 g/L, [DMPO] = [TEMP] = 60 mM, Irradiance = 35.85 mW/cm^2.

the presence of AAP (Fig. 5b–d), revealing that AAP reacts with h$^+$, i.e., it is oxidized by holes that cause an increase in the photo-current response (Fig. 5b–d).

Thus, based on all the above results, h$^+$, and O$_2^-$ were identified as the reactive species generated concomitantly in HT-g-C$_3$N$_4$/PS system that caused effective degradation of AAP (Eq. (13)).

Proposed mechanism:

$$HT - g - C_3N_4 \xrightarrow{h\nu} VB\ (h^+) + CB\ (e^-) \tag{6}$$

$$O_2 + CB\ (e^-) \rightarrow O_2^- \tag{7}$$

$$S_2O_8^{2-} + CB\ (e^-) \rightarrow \left[S_2O_8^{2-}\right]^- \tag{8}$$

$$\left[S_2O_8{}^{2-}\right]^- + O_2 \rightarrow S_2O_8{}^{2-} + O_2{}^- \tag{9}$$

$$S_2O_8{}^{2-} + CB\ (e^-) \rightarrow SO_4{}^{2-} + SO_4{}^- \tag{10}$$

$$SO_4{}^- + H_2O \rightarrow HO^{\cdot} + SO_4{}^{2-} + H^+ \tag{11}$$

$$SO_4{}^- + HO^- \rightarrow HO^{\cdot} + SO_4{}^{2-} \tag{12}$$

$$O_2{}^-, h^+ + AAP \rightarrow Intermediates + CO_2 + H_2O \tag{13}$$

3.6. Recyclability of HT-g-C₃N₄ photocatalyst

HT-g-C$_3$N$_4$ was reused five times (Fig. 15). The reused photocatalyst showed a slight decrease in the degradation efficiency of AAP (~10%) after the second cycle. The slight decrease in efficiency is attributed to the loss of photocatalyst during the centrifugal separation, and washing of the photocatalyst before reuse [55]. The above results reveal that HT-g-C$_3$N$_4$ photocatalyst possesses good stability and reusability (Fig. 15b–d).

3.7. Degradation of AAP using HT-g-C₃N₄/PS system in the different water matrix

Degradation of AAP in RO water may significantly differ from that in real waters, which contain significant concentrations of inorganic ions and organic compounds. Fig. 16a illustrates that the HT-g-C$_3$N$_4$/PS system achieved complete degradation of AAP in both simulated groundwater and real tap water. However, the k$_{obs}$ values obtained for simulated groundwater and real tap water were lower than the k$_{obs}$ value observed in RO water, namely 0.029 min^{-1} and 0.035 min^{-1} for simulated groundwater and real tap water, respectively, compared to 0.328 min^{-1} in RO water. This result is attributed to the presence of richly found inorganic anions and organic compounds in real tap waters as well as simulated groundwater [56,57].

The degradation efficiency of AAP in the presence of different inorganic anions are presented in Fig. 16b. The degradation efficiency follows the order (Cl$^-$ > NO$_3^-$ > SO$_4^{2-}$ > PO$_4^{3-}$ > HCO$_3^-$ > Resorcinol). The slight decrease in the degradation efficiency of AAP in the presence of Cl$^-$, may be attributed to the hole-scavenging property of Cl$^-$ [58]. The nitrates, sulphates and phosphate anions react with reactive radicals to generate a less reactive radicals with low-rate constants as reported earlier [59]. Hence, these anions have inhibition effect of AAP degradation [59]. However, the presence of HCO$_3^-$ has a detrimental effect on the degradation of AAP. HCO$_3^-$ was reported to be a well-known hole and radical scavenger [60,61]. The effect of resorcinol (a model for natural organic matter) [57,62] was found to adversely affect AAP degradation efficiency Fig. 16b. This fact can be attributed to the decrease in the solution transparency by resorcinol, thereby inhibiting the light penetration in the reaction solution [63]. Additionally, resorcinol is known to scavenge O$_2^-$ in hypoxanthine (HPX)-Xanthine oxidase system, as reported earlier [64]. Hence, the presence of resorcinol had a negative impact on the degradation efficiency of AAP.

3.8. Identification of intermediate product

The degradation pathway of AAP and their possible intermediate products were analyzed by LC-MS and is proposed in Fig. 17 [45, 65]. Around 40% total organic carbon (TOC) reduction is achieved within 3 h in HT-g-C$_3$N$_4$/PS system. The result indicates the slow mineralization and presence of possible degraded intermediates. This slow mineralization may be attributed to the stable dimer formation [45,66].

3.9. Evaluation of the ecotoxicity

Due to the possibility of by-products produced during pollutant degradation being more toxic than the original pollutants, it is important to investigate the ecotoxicity change of the pollutants and their degraded solutions. The Initial toxicity of AAP showed 37% bioluminescence inhibition towards aquatic bacteria *A. fischeri* (ATCC 7744) (Fig. 18). This result reveals that AAP was found to be toxic to *A. fischeri*. When AAP was degraded for 18 min by the HT-g-C$_3$N$_4$/PS system there was no bioluminescence inhibition, indicating the toxicity was completely removed after the photodegradation reaction. The removal of AAP toxicity towards *A. fischeri* after degradation has also been reported earlier [45].

3.10. Comparison of AAP degradation by previously reported photocatalyst/PS/light systems

Earlier reports on degradation of AAP by various photocatalyst/PS/light systems were summarized in Table S5 [3,45,67,68]. The modification of g-C$_3$N$_4$ performed in the present study involves simple hydrothermal treatment at neutral pH without use of additional chemicals. The k$_{obs}$ value for degradation of AAP by the proposed HT-g-C$_3$N$_4$/PS system was higher than g-C$_3$N$_4$/PS system. Overall, the k$_{obs}$ value indicates HT-g-C$_3$N$_4$/PS is a promising system for degradation of AAP.
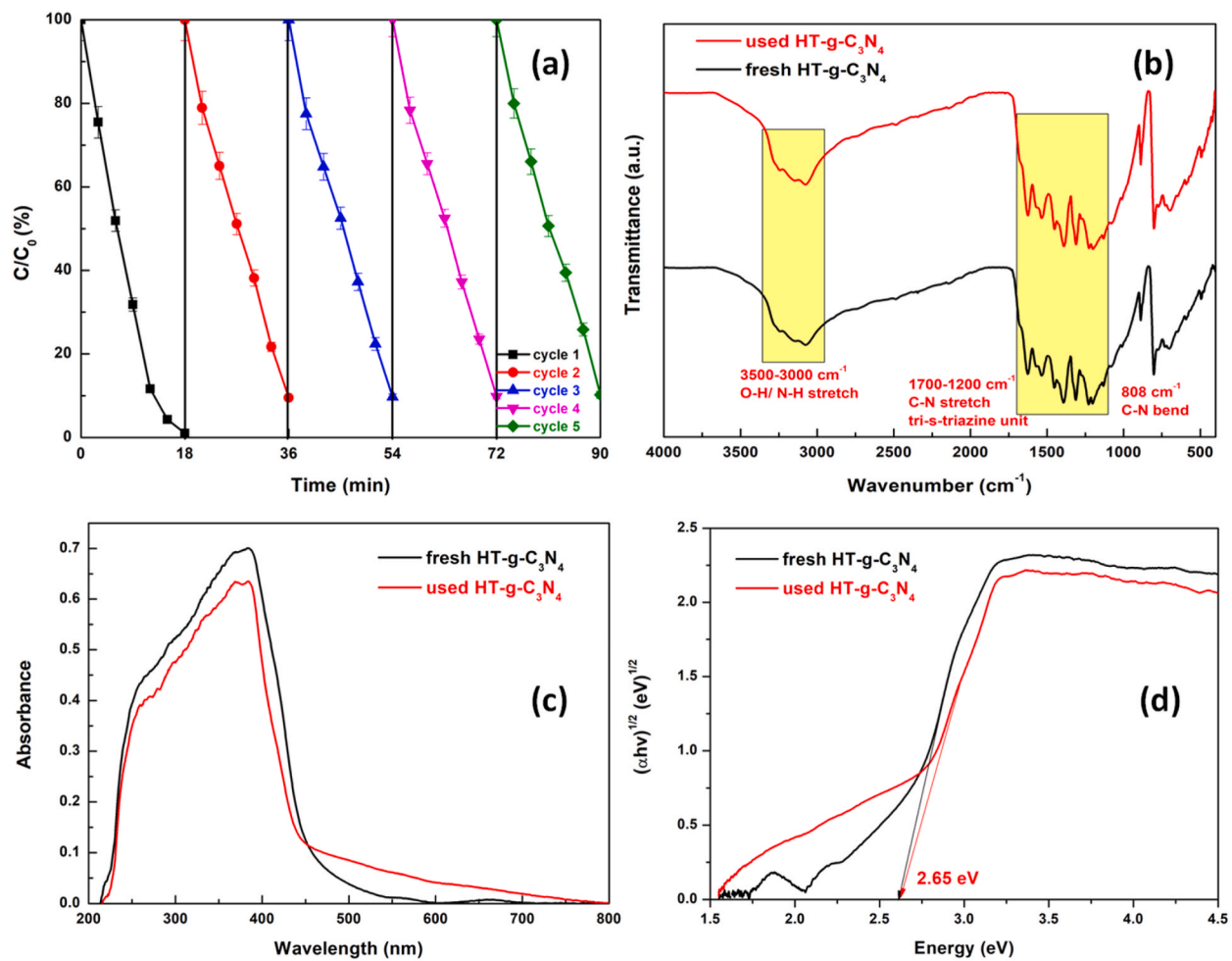
Fig. 15. (a) Recyclability of HT-g-C_3N_4 photocatalyst for AAP degradation; [AAP] = 10 ppm, [PS] = 0.6 mM, [HT-g-C_3N_4] = 0.4 g/L, Irradiance = 35.85 mW/cm^2 (b) FT-IR (c) UV-DRS, and (d) Tauc's plot of fresh HT-g-C_3N_4 and used HT-g-C_3N_4 (after 5 cycles).
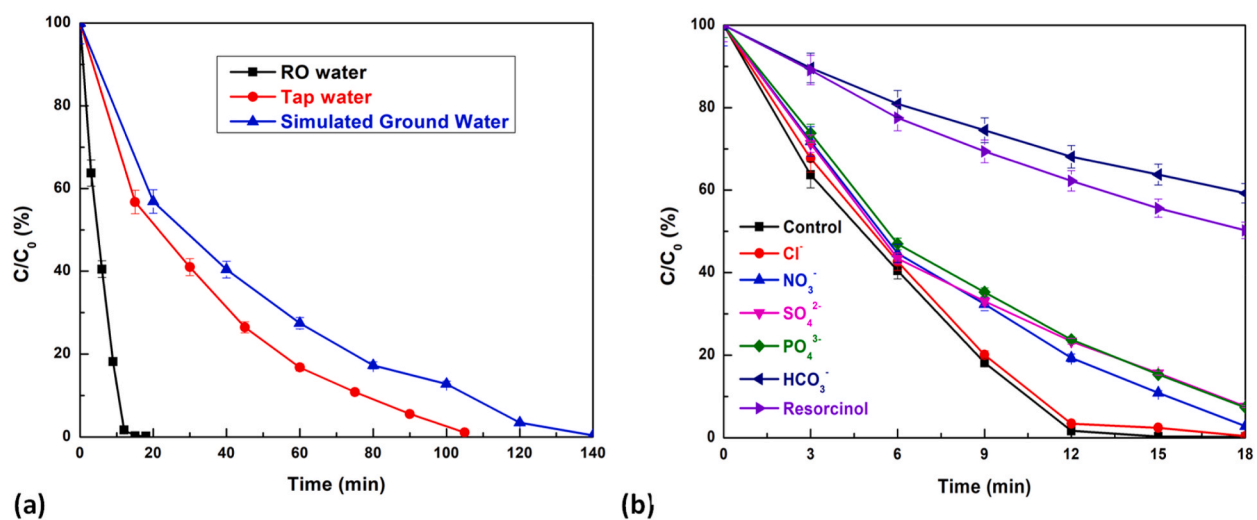

Fig. 16. (a) Influence of water matrix on AAP degradation; (b) Effects of inorganic anions on AAP degradation [AAP] = 10 ppm, [PS] = 0.6 mM, [HT-g-C_3N_4] = 0.4 g/L, [Cl^-] = [NO_3^-] = [SO_4^{2-}] [PO_4^{3-}] = [HCO_3^-] = [Resorcinol] = 1 mM, Irradiance = 35.85 mW/cm^2.
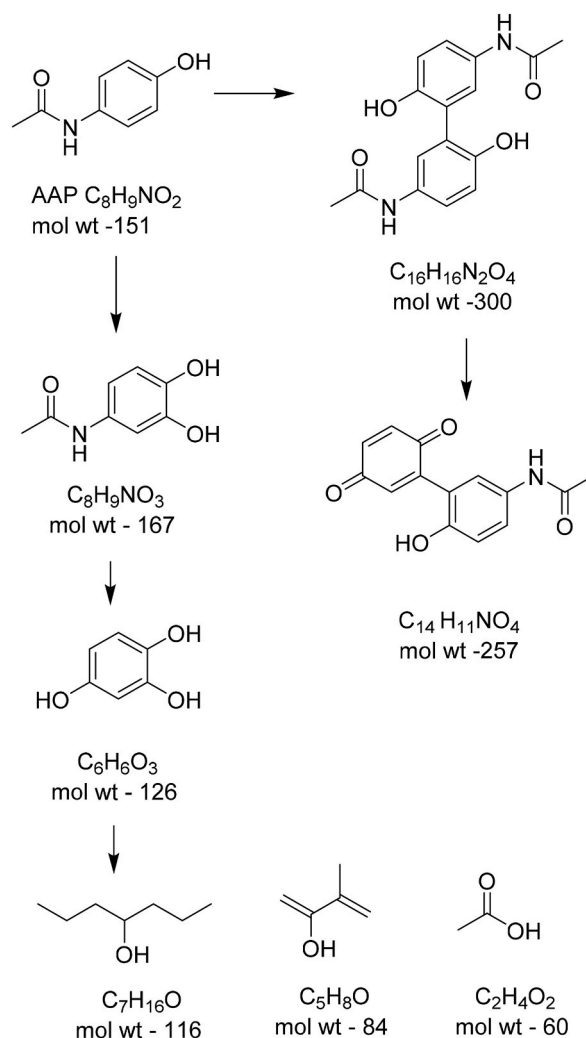
Fig. 17. Possible degradation pathways of AAP in the HT-g-C_3N_4/PS system.

4. Conclusion

The HT-g-C_3N_4/PS system demonstrated a k_{obs} value for the photocatalytic degradation of AAP that was 15 times higher than that of the g-C_3N_4/PS system. Radical scavenging experiment and ESR results reveals O_2^- and h^+ reactive species are significant compared to $^1O_2$, SO_4^- and $HO^.$ reactive species in HT-g-C_3N_4/PS system for degradation of AAP. The electron-hole pair recombination in HT-g-C_3N_4 is retarded compared to g-C_3N_4, which favors the HT-g-C_3N_4 photocatalysis. PS acts as a redox mediator and promote O_2^- formation. HT-g-C_3N_4 photocatalyst showed a high photocurrent response in the presence of AAP, revealing that h^+ has the ability to oxidize AAP. Moreover, the HT-g-C_3N_4 showed recyclability and stability for five cycles. The possible degradation pathway of AAP is proposed. The degraded AAP solution showed no toxicity towards marine bacteria *A. fischeri*. Overall, the present findings highlight a new HT-g-C_3N_4/PS system, with potential to emerge as a sustainable and effective photocatalytic technology for water treatment.

Author contribution statement

Smita Gupta: Conceived and designed the experiments; Performed the experiments; Analyzed and interpreted the data; Wrote the paper.

Jemi Gandhi, Santosh Kokate, Laxman G. Raikar: Performed the experiments; Analyzed and interpreted the data.

Vijayakumar Gupta Kopuri: Contributed reagents, materials, analysis tools or data.

Halan Prakash: Conceived and designed the experiments; Analyzed and interpreted the data; Contributed reagents, materials, analysis tools or data; Wrote the paper.
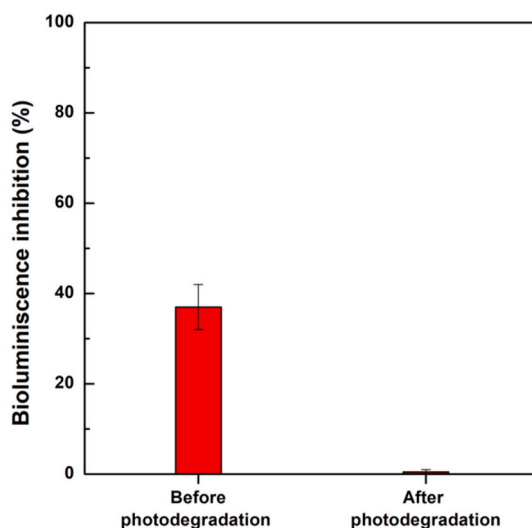
Fig. 18. Changes in ecotoxicity before and after photodegradation of AAP [AAP] = 10 ppm, [PS] = 0.6 mM, [HT-g-C$_3$N$_4$] = 0.4 g/L, Irradiance = 35.85 mW/cm^2.

Data availability statement

Data will be made available on request.

Declaration of competing interest

The authors declare that they have no known competing financial interests or personal relationships that could have appeared to influence the work reported in this paper.

Acknowledgments

Appendix A. Supplementary data

Supplementary data to this article can be found online at https://doi.org/10.1016/j.heliyon.2023.e16450.

References

[1] M.F. Meyer, S.M. Powers, S.E. Hampton, An evidence synthesis of pharmaceuticals and personal care products (PPCPs) in the environment: imbalances among compounds, sewage treatment techniques, and ecosystem types, Environ. Sci. Technol. 53 (22) (2019) 12961–12973, https://doi.org/10.1021/acs.est.9b02966.

[2] H.N.P. Vo, et al., Acetaminophen micropollutant: historical and current occurrences, toxicity, removal strategies and transformation pathways in different environments, Chemosphere 236 (2019), 124391, https://doi.org/10.1016/j.chemosphere.2019.124391.

[3] M. Noorisepehr, et al., Sulfate radical-based oxidative degradation of acetaminophen over an efficient hybrid system: peroxydisulfate decomposed by ferroferric oxide nanocatalyst anchored on activated carbon and UV light, Sep. Purif. Technol. 250 (2020), 116950, https://doi.org/10.1016/j.seppur.2020.116950.

[4] B. Kasprzyk-Hordern, R.M. Dinsdale, A.J. Guwy, The occurrence of pharmaceuticals, personal care products, endocrine disruptors and illicit drugs in surface water in South Wales, UK, Water Res. 42 (13) (2008) 3498–3518, https://doi.org/10.1016/j.watres.2008.04.026.

[5] R.C. Dart, E.K. Kuffner, B.H. Rumack, Treatment of pain or fever with paracetamol (acetaminophen) in the alcoholic patient: a systemic review, Am. J. Therapeut. 7 (2) (2000) 123–134.

[6] C.-C. Su, et al., Effect of UV light on acetaminophen degradation in the electro-Fenton process, Sep. Purif. Technol. 120 (2013) 43–51, https://doi.org/10.1016/j.seppur.2013.09.034.

[7] R.A. Granberg, Å.C. Rasmuson, Solubility of paracetamol in pure solvents, J. Chem. Eng. Data 44 (6) (1999) 1391–1395, https://doi.org/10.1021/je990124v.

[8] C. Tan, et al., *Radical induced degradation of acetaminophen with Fe$_3$O$_4$ magnetic nanoparticles as heterogeneous activator of peroxymonosulfate*, J. Hazard Mater. 276 (2014) 452–460, https://doi.org/10.1016/j.jhazmat.2014.05.068.

[9] Y. Kim, et al., Aquatic toxicity of acetaminophen, carbamazepine, cimetidine, diltiazem and six major sulfonamides, and their potential ecological risks in Korea, Environ. Int. 33 (3) (2007) 370–375, https://doi.org/10.1016/j.envint.2006.11.017.

[10] M. Bedner, W.A. MacCrehan, Transformation of acetaminophen by chlorination produces the toxicants 1, 4-benzoquinone and N-acetyl-p-benzoquinone imine, Environ. Sci. Technol. 40 (2) (2006) 516–522, https://doi.org/10.1021/es0509073.

[11] T.O. Ajiboye, A.T. Kuvarega, D.C. Onwudiwe, Graphitic carbon nitride-based catalysts and their applications: a review, Nano-Structures & Nano-Objects 24 (2020), 100577, https://doi.org/10.1016/j.nanoso.2020.100577.

[12] Y. Tao, et al., *Metal-free activation of peroxymonosulfate by g-C₃N₄ under visible light irradiation for the degradation of organic dyes*, RSC Adv. 5 (55) (2015) 44128–44136, https://doi.org/10.1039/C5RA06223C.

[13] H. Yan, et al., *In-situ intercalation of MoO₃₋ₓ in g-C₃N₄ for the enhancement of photocatalytic and antibacterial activities*, J. Photochem. Photobiol. Chem. 390 (2020), 112297, https://doi.org/10.1016/j.jphotochem.2019.112297.

[14] C. Tang, et al., *Nontoxic carbon quantum dots/g-C₃N₄ for efficient photocatalytic Inactivation of Staphylococcus aureus under visible light*, Adv. Healthcare Mater. 8 (10) (2019), 1801534, https://doi.org/10.1002/adhm.201801534.

[15] J. Tan, et al., Graphitic carbon nitride-based materials in activating persulfate for aqueous organic pollutants degradation: a review on materials design and mechanisms, Chemosphere 262 (2021), 127675, https://doi.org/10.1016/j.chemosphere.2020.127675.

[16] T. Sano, et al., *Activation of graphitic carbon nitride (g-C₃N₄) by alkaline hydrothermal treatment for photocatalytic NO oxidation in gas phase*, J. Mater. Chem. 1 (21) (2013) 6489–6496. https://pubs.rsc.org/en/content/articlehtml/2013/ta/c3ta10472a.

[17] B. Liu, et al., *Persulfate enhanced photocatalytic degradation of bisphenol A by g-C₃N₄ nanosheets under visible light irradiation*, Chemosphere 189 (2017) 115–122, https://doi.org/10.1016/j.chemosphere.2017.08.169.

[18] X. Jiang, et al., *The photocatalytic performance of g-C₃N₄ from melamine hydrochloride for dyes degradation with peroxymonosulfate*, J. Photochem. Photobiol. Chem. 336 (2017) 54–62, https://doi.org/10.1016/j.jphotochem.2016.12.018.

[19] S. Kokate, et al., *Energy efficient photocatalytic activation of peroxymonosulfate by g-C₃N₄ under 400 nm LED irradiation for degradation of Acid Orange 7*, Chemosphere 287 (2022), 132099, https://doi.org/10.1016/j.chemosphere.2021.132099.

[20] W.-K. Jo, R.J. Tayade, New generation energy-efficient light source for photocatalysis: LEDs for environmental applications, Ind. Eng. Chem. Res. 53 (6) (2014) 2073–2084, https://doi.org/10.1021/ie404176e.

[21] L. Svoboda, et al., Graphitic carbon nitride nanosheets as highly efficient photocatalysts for phenol degradation under high-power visible LED irradiation, Mater. Res. Bull. 100 (2018) 322–332, https://doi.org/10.1016/j.materresbull.2017.12.049.

[22] B. Zhu, et al., *Isoelectric point and adsorption activity of porous g-C₃N₄*, Appl. Surf. Sci. 344 (2015) 188–195, https://doi.org/10.1016/j.apsusc.2015.03.086.

[23] M. Cui, et al., Synergistic effect of mesoporous graphitic carbon nitride and peroxydisulfate in visible light-induced degradation of atenolol: a combined experimental and theoretical study, Chem. Eng. J. 412 (2021), 127979, https://doi.org/10.1016/j.cej.2020.127979.

[24] J. Qin, et al., Direct growth of uniform carbon nitride layers with extended optical absorption towards efficient water-splitting photoanodes, Nat. Commun. 11 (1) (2020) 1–9, https://doi.org/10.1038/s41467-020-18535-0.

[25] H. Shao, et al., *Enhanced photoelectrocatalytic degradation of bisphenol a by BiVO₄ photoanode coupling with peroxymonosulfate*, J. Hazard Mater. 394 (2020), 121105, https://doi.org/10.1016/j.jhazmat.2019.121105.

[26] K. Gelderman, L. Lee, S. Donne, Flat-band potential of a semiconductor: using the Mott–Schottky equation, J. Chem. Educ. 84 (4) (2007) 685, https://doi.org/10.1021/ed084p685.

[27] A. Hankin, et al., Flat band potential determination: avoiding the pitfalls, J. Mater. Chem. 7 (45) (2019) 26162–26176, https://doi.org/10.1039/C9TA09569A.

[28] L. Wang, C.-Y. Lee, P. Schmuki, *Solar water splitting: preserving the beneficial small feature size in porous α-Fe₂O₃ photoelectrodes during annealing*, J. Mater. Chem. 1 (2) (2013) 212–215, https://doi.org/10.1039/C2TA00431C.

[29] Y. Liu, et al., Aminobenzaldehyde convenletly modified graphitic carbon nitride photocatalyst through Schiff base reaction: regulating electronic structure and improving visible-light-driven photocatalytic activity for moxifloxacin degradation, J. Colloid Interface Sci. 630 (2023) 867–878, https://doi.org/10.1016/j.jcis.2022.10.073.

[30] G. Subramanian, P. Parakh, H. Prakash, Photodegradation of methyl orange and photoinactivation of bacteria by visible light activation of persulphate using a tris (2, 2′-bipyridyl) ruthenium (ii) complex, Photochem. Photobiol. Sci. 12 (3) (2013) 456–466, https://doi.org/10.1039/C2PP25316J.

[31] M. Abbas, et al., Vibrio fischeri bioluminescence inhibition assay for ecotoxicity assessment: a review, Sci. Total Environ. 626 (2018) 1295–1309, https://doi.org/10.1016/j.scitotenv.2018.01.066.

[32] H. Nie, et al., *Efficient visible-light photocatalytic oxidation of gaseous NO with graphitic carbon nitride (g-C₃N₄) activated by the alkaline hydrothermal treatment and mechanism analysis*, J. Hazard Mater. 300 (2015) 598–606, https://doi.org/10.1016/j.jhazmat.2015.07.066.

[33] Y. Liao, et al., A facile method of activating graphitic carbon nitride for enhanced photocatalytic activity, Phys. Chem. Chem. Phys. 17 (41) (2015) 27826–27832, https://doi.org/10.1039/C5CP05186J.

[34] L. Liu, et al., Synthesis and characterization of microporous carbon nitride, Microporous Mesoporous Mater. 110 (2–3) (2008) 216–222, https://doi.org/10.1016/j.micromeso.2007.06.012.

[35] M. Green, et al., Graphitic carbon nitride nanosheets for microwave absorption, Mater. Today Phys. 5 (2018) 78–86, https://doi.org/10.1016/j.mtphys.2018.06.005.

[36] F. Dong, et al., Engineering the nanoarchitecture and texture of polymeric carbon nitride semiconductor for enhanced visible light photocatalytic activity, J. Colloid Interface Sci. 401 (2013) 70–79, https://doi.org/10.1016/j.jcis.2013.03.034.

[37] L. Ming, et al., *Hydrothermal synthesis of oxidized g-C₃N₄ and its regulation of photocatalytic activity*, J. Mater. Chem. 2 (45) (2014) 19145–19149, https://doi.org/10.1039/C4TA04041D.

[38] L. Mao, et al., *Rapid high-temperature hydrothermal post treatment on graphitic carbon nitride for enhanced photocatalytic H₂ evolution*, Catal. Today 409 (2023) 94–102, https://doi.org/10.1016/j.cattod.2022.03.035.

[39] G. Xu, et al., Facile hydrothermal preparation of graphitic carbon nitride supercell structures with enhanced photodegradation activity, Diam. Relat. Mater. 97 (2019), 107461, https://doi.org/10.1016/j.diamond.2019.107461.

[40] S. Kodama, et al., Surface modification of adsorbents by dielectric barrier discharge, Thin Solid Films 407 (1–2) (2002) 151–155, https://doi.org/10.1016/S0040-6090(02)00030-5.

[41] D.I. Patel, et al., Water vapor, by near-ambient pressure XPS, Surf. Sci. Spectra 26 (1) (2019), 014026, https://doi.org/10.1116/1.5111634.

[42] A.W. Bott, Electrochemistry of semiconductors, Curr. Sep. 17 (1998) 87–92.

[43] F. Mo, et al., Photocatalytic elimination of moxifloxacin by two-dimensional graphitic carbon nitride nanosheets: enhanced activity, degradation mechanism and potential practical application, Sep. Purif. Technol. 292 (2022), 121067, https://doi.org/10.1016/j.seppur.2022.121067.

[44] C. Liang, H.-W. Su, Identification of sulfate and hydroxyl radicals in thermally activated persulfate, Ind. Eng. Chem. Res. 48 (11) (2009) 5558–5562, https://doi.org/10.1021/ie9002848.

[45] X. Du, et al., *Visible-light activation of persulfate by TiO₂/g-C₃N₄ photocatalyst toward efficient degradation of micropollutants*, Chem. Eng. J. 384 (2020), 123245, https://doi.org/10.1016/j.cej.2019.123245.

[46] R.R. Solís, Ö. Dinc, G. Fang, M.N. Nadagouda, D.D. Dionysiou, Activation of inorganic peroxides with magnetic graphene for the removal of antibiotics from wastewater, Environ. Sci. Nano 8 (2021) 960–977, https://doi.org/10.1039/D0EN01280G.

[47] L. Bu, et al., Degradation of oxcarbazepine by UV-activated persulfate oxidation: kinetics, mechanisms, and pathways, Environ. Sci. Pollut. Control Ser. 23 (3) (2016) 2848–2855, https://doi.org/10.1007/s11356-015-5524-1.

[48] M.O. Alfred, et al., *Sunlight-active Cu/Fe@ ZnWO₄-kaolinite composites for degradation of acetaminophen, ampicillin and sulfamethoxazole in water*, Ceram. Int. 47 (13) (2021) 19220–19233, https://doi.org/10.1016/j.ceramint.2021.03.219.

[49] X. Zhang, et al., *Photodegradation of acetaminophen in TiO₂ suspended solution*, J. Hazard Mater. 157 (2–3) (2008) 300–307, https://doi.org/10.1016/j.jhazmat.2007.12.098.

[50] J. Meng, et al., Engineering of graphitic carbon nitride with simultaneous potassium doping sites and nitrogen defects for notably enhanced photocatalytic oxidation performance, Sci. Total Environ. 796 (2021), 148946, https://doi.org/10.1016/j.scitotenv.2021.148946.

[51] S. Cheeseman, et al., Antimicrobial metal nanomaterials: from passive to stimuli-activated applications, Adv. Sci. 7 (10) (2020), 1902913, https://doi.org/10.1002/advs.201902913.

[52] Y. Song, et al., *Synergistic effect of persulfate and g-C3N4 under simulated solar light irradiation: Implication for the degradation of sulfamethoxazole*, J. Hazard Mater. 393 (2020), 122379, https://doi.org/10.1016/j.jhazmat.2020.122379.

[53] M.J. Davies, et al., Nucleophilic substitution reactions of spin adducts. Implications for the correct identification of reaction intermediates by EPR/spin trapping, J. Chem. Soc. Perkin Trans. 2 (3) (1992) 333–335, https://doi.org/10.1039/P29920000333.

[54] X. Cheng, et al., Non-photochemical production of singlet oxygen via activation of persulfate by carbon nanotubes, Water Res. 113 (2017) 80–88, https://doi.org/10.1016/j.watres.2017.02.016.

[55] M. Tobajas, C. Belver, J. Rodriguez, *Degradation of emerging pollutants in water under solar irradiation using novel TiO2-ZnO/clay nanoarchitectures*, Chem. Eng. J. 309 (2017) 596–606, https://doi.org/10.1016/j.cej.2016.10.002.

[56] J. Marugán, et al., Kinetics of the photocatalytic disinfection of Escherichia coli suspensions, Appl. Catal. B Environ. 82 (1–2) (2008) 27–36, https://doi.org/10.1016/j.apcatb.2008.01.002.

[57] E. Ortega-Gómez, et al., Solar photo-Fenton for water disinfection: an investigation of the competitive role of model organic matter for oxidative species, Appl. Catal. B Environ. 148 (2014) 484–489, https://doi.org/10.1016/j.apcatb.2013.09.051.

[58] A.M. Dugandžić, et al., Effect of inorganic ions, photosensitisers and scavengers on the photocatalytic degradation of nicosulfuron, J. Photochem. Photobiol. Chem. 336 (2017) 146–155, https://doi.org/10.1016/j.jphotochem.2016.12.031.

[59] J. Wang, S. Wang, Effect of inorganic anions on the performance of advanced oxidation processes for degradation of organic contaminants, Chem. Eng. J. 411 (2021), 128392, https://doi.org/10.1016/j.cej.2020.128392.

[60] C.-R. Zhong, et al., Origin of the enhanced photocatalytic activity of graphitic carbon nitride nanocomposites and the effects of water constituents, Carbon 167 (2020) 852–862, https://doi.org/10.1016/j.carbon.2020.06.028.

[61] B. Gao, et al., *Adsorption-photocatalytic degradation of Acid Red 88 by supported TiO2: Effect of activated carbon support and aqueous anions*, Chem. Eng. J. 171 (3) (2011) 1098–1107, https://doi.org/10.1016/j.cej.2011.05.006.

[62] D. Spuhler, J.A. Rengifo-Herrera, C. Pulgarin, *The effect of Fe2+, Fe3+, H2O2 and the photo-Fenton reagent at near neutral pH on the solar disinfection (SODIS) at low temperatures of water containing Escherichia coli K12*, Appl. Catal. B Environ. 96 (1–2) (2010) 126–141, https://doi.org/10.1016/j.apcatb.2010.02.010.

[63] A. Shad, et al., *Degradation of sulfadimethoxine in phosphate buffer solution by UV alone, UV/PMS and UV/H2O2: kinetics, degradation products, and reaction pathways*, Chem. Eng. J. 398 (2020), 125357, https://doi.org/10.1016/j.cej.2020.125357.

[64] S. Kitagawa, H. Fujisawa, H. Sakurai, Scavenging effects of dihydric and polyhydric phenols on superoxide anion radicals, studied by electron spin resonance spectrometry, Chem. Pharm. Bull. 40 (2) (1992) 304–307, https://doi.org/10.1248/cpb.40.304.

[65] G. Fan, et al., Degradation of acetaminophen in aqueous solution under visible light irradiation by Bi-modified titanate nanomaterials: morphology effect, kinetics and mechanism, Catal. Sci. Technol. 8 (22) (2018) 5906–5919, https://doi.org/10.1039/C8CY01614C.

[66] H. Xiao, et al., Transformation of acetaminophen using manganese dioxide− mediated oxidative processes: reaction rates and pathways, J. Hazard Mater. 250 (2013) 138–146, https://doi.org/10.1016/j.jhazmat.2013.01.070.

[67] R.S. Kumar, et al., *Fe3O4 nanorods decorated on polypyrrole/reduced graphene oxide for electrochemical detection of dopamine and photocatalytic degradation of acetaminophen*, Appl. Surf. Sci. 556 (2021), 149765, https://doi.org/10.1016/j.apsusc.2021.149765.

[68] X. Wang, et al., *Degradation of Acetaminophen via UVA-induced advanced oxidation processes (AOPs). Involvement of different radical species: HO·, SO4− and HO2/O2−* Chemosphere 258 (2020), 127268, https://doi.org/10.1016/j.chemosphere.2020.127268.

[69] S. Zhang, C. Hu, H. Ji, L. Zhang, F. Li, Facile synthesis of nitrogen-deficient mesoporous graphitic carbon nitride for highly efficient photocatalytic performance, Appl. Surf. Sci. 478 (2019) 304–312. https://doi.org/10.1016/j.apsusc.2019.01.270.